ELECTRON-SELECTIVE CONTACTS FOR N-TYPE CRYSTALLINE SILICON SOLAR CELLS: A STUDY ON AN ULTRATHIN ZIRCONIUM OXIDE LAYER

A THESIS SUBMITTED TO
THE GRADUATE SCHOOL OF NATURAL AND APPLIED SCIENCES
OF
MIDDLE EAST TECHNICAL UNIVERSITY

BY

LOAY AKMAL MOSTAFA KAMAL MADBOULY

IN PARTIAL FULFILLMENT OF THE REQUIREMENTS
FOR
THE DEGREE OF MASTER OF SCIENCE
IN
METALLURGICAL AND MATERIALS ENGINEERING

SEPTEMBER 2022

Approval of the thesis:

ELECTRON-SELECTIVE CONTACTS FOR N-TYPE CRYSTALLINE SILICON SOLAR CELLS: A STUDY ON AN ULTRATHIN ZIRCONIUM OXIDE LAYER

submitted by **LOAY AKMAL MOSTAFA KAMAL MADBOULY** in partial fulfillment of the requirements for the degree of **Master of Science** in **Metallurgical and Materials Engineering**, **Middle East Technical University** by,

Prof. Dr. Halil Kalıpçılar
Dean, Graduate School of **Natural and Applied Sciences** ____________________

Prof. Dr. Ali Kalkanlı
Head of the Department, Metallurgical and Materials Eng. ____________________

Prof. Dr. Hüsnü Emrah Ünalan
Supervisor, Metallurgical and Materials Eng. ____________________

Prof. Dr. Raşit Turan
Co-Supervisor, Physics ____________________

Examining Committee Members:

Prof. Dr. Akin Bacioğlu
Physics Eng., Hacettepe University ____________________

Prof. Dr. Hüsnü Emrah Ünalan
Metallurgical and Materials Eng., METU ____________________

Prof. Dr. Raşit Turan
Physics, METU ____________________

Assoc. Prof. Dr. Selçuk Yerci
Electrical and Electronics Eng., METU ____________________

Assist. Prof. Dr. Yusuf Keleştemur
Metallurgical and Materials Eng., METU ____________________

Defense Date: 02.09.2022

I hereby declare that all information in this document has been obtained and presented in accordance with academic rules and ethical conduct. I also declare that, as required by these rules and conduct, I have fully cited and referenced all material and results that are not original to this work.

Name, Last name: Loay Akmal Madbouly

Signature:

ABSTRACT

ELECTRON-SELECTIVE CONTACTS FOR N-TYPE CRYSTALLINE SILICON SOLAR CELLS: A STUDY ON AN ULTRATHIN ZIRCONIUM OXIDE LAYER

Madbouly, Loay Akmal
Master of Science, Metallurgical and Materials Engineering
Supervisor: Prof. Dr. Hüsnü Emrah Ünalan
Co-Supervisor: Prof. Dr. Raşit Turan

September 2022, 87 pages

Crystalline silicon (c-Si) solar cell efficiencies have peaked at around 26%. To get closer and even go beyond the Shockley-Queisser Limit, passivation of the rear contact of c-Si solar cells is mandatory. Formation of ohmic, low-resistance and economically feasible contacts is impeded by the fermi-level pinning phenomenon in lightly doped n-type c-Si (n-Si). Over the past two decades, much research has been done to find materials that can replace the commonly used silicon dioxide (SiO_2) as it showed electrical instabilities at low thicknesses in microelectronic applications.

Zirconium dioxide (ZrO_2) is potentially capable of succeeding SiO_2 due to its high dielectric constant, large band gap, environmental stability, high service temperature, electron-selective nature, and lattice constant match with Si. It can also be easily deposited using solution-based techniques or vacuum systems. ZrO_2 is also economically viable to purchase and process.

To understand and analyze the interactions between ZrO_2 and c-Si, experiments were conducted with different deposition techniques. While reaching the required nanoscale thickness of ZrO_2 layer was challenging using solution processing techniques (such as spin coating and spray coating), vacuum-based deposition

techniques (such as thermal and electron-beam evaporation) were able to deposit ZrO_x layers on c-Si with a thickness of 1 nm.
Following successful deposition of the 1 nm thick ZrO_x passivation layer on c-Si, it was profoundly characterized by X-Ray photoelectron spectroscopy (XPS), X-Ray diffraction (XRD) analysis, transmission electron microscopy (TEM) and spectroscopic ellipsometry (SE).
Afterwards, the effect of passivation was investigated by conducting contact resistivity (ρ_c) measurements, using Cox-Strack method (CSM), for different thickness on n-Si wafers with different resistivities. ZrO_x was deposited through e-beam evaporation at room temperature. The contact resistivity was found to be highly dependent on the ZrO_x thickness. The lowest ρ_c obtained using only 1 nm thick ZrO_x was 21 mΩ.cm^2. Moreover, the electron-selective nature of ZrO_x was proven by CSM as it showed ohmic behavior when it was deposited as an interlayer between n-Si and aluminum (Al).

As a proof of concept, an n-Si solar cell was fabricated with 1 nm ZrO_x deposited at its rear contact to elucidate the effect of ZrO_x passivation on the performance of n-Si solar cell. 1 nm thick ZrO_x rear-contact-passivated n-Si solar cell showed significant performance with a short circuit current density (J_{SC}) of 33.86 mA/mm^2, an open circuit voltage (V_{OC}) of 600.0 mV, a fill factor (FF) of 79.1% and an overall efficiency (η) of 16.1%. These values successfully demonstrate the use of ZrO_x with Al as an emerging electron-selective layer contact for lightly doped n-Si wafers.

Keywords: Zirconium Oxide, Crystalline Silicon Solar Cells, Passivation, Contacts, Renewable Energy

ÖZ

ELEKTRON-TAŞIYICI KONTAKTLAR N-TIPI KRİSTAL SİLİKON GÜNEŞ HÜCRELERİ İÇİN: ULTRA İNCE ZİRKONYUM OKSİT KATMANI ÜZERİNE BİR ÇALIŞMA

Madbouly, Loay Akmal
Yüksek Lisans, Metalurji ve Malzeme Mühendisliği
Tez Yöneticisi: Prof. Dr. Hüsnü Emrah Ünalan
Ortak Tez Yöneticisi: Prof. Dr. Raşit Turan

Eylül 2022, 87 sayfa

Kristal silisyum (c-Si) güneş pillerinin verimliliği yaklaşık %26'ya ulaşmıştır. Shockley-Queisser limitine yaklaşmak ve hatta ötesine geçmek için c-Si güneş hücrelerinin arka kontakt pasifleştirilmesi zorunludur. Hafif katkılı n-tipi c-Si'de Ohmik, düşük dirençli ve ekonomik olarak uygun kontakların oluşumu fermi-seviye pinleme fenomeni tarafından engellenir. Son yirmi yılda yaygın olarak kullanılan silisyum dioksitin (SiO_2) yerini alabilecek malzemeleri bulmak için birçok araştırma yapılmıştır çünkü SiO_2 mikroelektronik uygulamalarda düşük kalınlıklarda elektriksel kararsızlıklar göstermektedir.

Zirkonyum dioksit (ZrO_2), yüksek dielektrik sabiti, geniş bant aralığı, çevresel kararlılığı, yüksek servis sıcaklığı, elektron seçici doğası ve Si ile örgü sabiti eşleşmesi nedeniyle potansiyel olarak SiO_2'nin yerine geçme potansiyeline sahiptir. Ayrıca, çözelti bazlı teknikler veya vakum sistemleri kullanılarak kolayca biriktirilebilir ve ZrO_2 satın alma ve işleme açısında ekonomik olarak uygundur.

ZrO_2'nin c-Si ile etkileşimini anlamak ve analiz etmek için farklı biriktirme teknikleri ile çalışmalar yapıldı. ZrO_2 tabakasının gerekli nano ölçekli kalınlığına

ulaşmak, çözelti işleme tekniklerini (döndürerek kaplama ve sprey kaplama gibi) kullanarak zor olsa da, vakuma dayalı biriktirme teknikleri (termal ve elektron ışını buharlaştırma gibi) 1 nm kalınlığında ZrO_x katmanını c-Si üzerinde biriktirebildi.

1 nm kalınlığındaki ZrO_x pasivasyon katmanının c-Si üzerine başarılı bir şekilde biriktirilmesinin ardından, X-ışını fotoelektron spektroskopisi (XPS), x-ışını kırınımı (XRD), transmisyon elektron mikroskobu (TEM), spektroskopik elipsometrisi (SE) ile derinlemesine karakterize edildi.

Daha sonra, farklı kalınlıklardaki farklı özdirençlere sahip n-tipi c-Si (n-Si) levhalar üzerinde için Cox-Strack yöntemi (CSM) ile temas özdirenci (ρ_c) ölçümleri yapılarak pasivasyonun etkisi araştırılmıştır. ZrO_x, oda sıcaklığında e-ışınlı buharlaştırma yöntemi ile biriktirildi. Kontakt direncinin, ZrO_x kalınlığına büyük ölçüde bağlı olduğu bulundu. Yalnızca 1 nm kalınlığında ZrO_x kullanılarak en düşük 21 mΩ.cm^2 ρ_C değeri elde edildi Ayrıca, ZrO_x'in elektron seçici doğası, n-Si ve alüminyum arasında bir ara katman olarak biriktirildiğinde Ohmik davranış gösterdiği için CSM tarafından kanıtlanmıştır.

Konseptin bir kanıtı olarak, ZrO_x pasivasyonunun n-Si güneş pilinin performansı üzerindeki etkisini açıklamak için arka kontaktında biriken 1 nm ZrO_x ile bir n-Si güneş hücresi üretildi.

1 nm kalınlığında ZrO_x arka kontakt pasifleştirilmiş n-Si güneş hücresi, kısa devre akım yoğunluğu (J_{SC}) 33.86 mA/mm^2, açık devre voltajı (V_{OC}) 600.0 mV, doldurma faktörü (FF) %79,1 ve toplam verimlilik (η) %16,1 ile önemli performans gösterdi. Bu değerler, hafif katkılı n-Si gofretler için ortaya çıkan elektron seçici katman teması olarak ZrO_x'un kullanımını başarılı bir şekilde göstermektedir.

Anahtar Kelimeler: Zirkonyum dioksit, Kristal silisyum güneş pilleri, Pasifleştirici kontak, Kontaklar, Yenilenebilir enerji

To the **courageous**,

ACKNOWLEDGMENTS

Professor Emrah Ünalan, thank you for the motivation, inspiration and care you showed towards me and everyone around you. Thank you for watching out for all of us when our indiscretion and/or circumstances got the best of us. Thank you for asking about our lives and health before asking about work and experiments. I'm deeply grateful and honored to be your student. Professor Rasit, thank you for trusting in me and teaching me, and thank you for your patience, care, and continuous support.

To my family, my parents, siblings, and brothers-in-law, thank you for everything.

Omar Mostafa, thank you for letting me know that the world won't (probably) end if I couldn't finish. Basil Eldeeb, thank you for helping me find the right answers regarding physics. Zeynep Kap, thank you for teaching me XPS and thank you for the uplifting talks. Dr. Alptekin Aydınlı, Dr. Ayran Azad, and Gamze Kökbudak, thank you for the immense care you showed towards me.

To all Nanolab family: Dr. Şahin Coşkun, Dr. Duygu Tan, Dr. Asude Çetin, Dr. Yaqoob Khan, Serkan Koylan, Yusuf Tutel, M. Batuhan Durukan, Deniz Keskin, M. Caner Görür, Onuralp Çakır, Şensu Tunca, Onur Demircıoğlu, M. Ögeday Çiçek, Murathan Cugunlular, Doğa Doganay, Sümeyye Kandur, Öykü Çetin, Ali Deniz Uçar, Tufan Bölükbaşı, Merve Güven, and Ahmet Keskin, thank you all for the loving, caring, and productive enviroment. Working with you is a blast!

Dr. Hisham Nasser, Dr. Mona Borra, Naser Beyraghi, Konstantin Tsoi, Milad Ghassani, Gökhan Altiner, and Tunç Bektaş, and the rest of ODTU-GUNAM members, thank you all.

This work was funded by the Scientific and Technological Research Council of Turkey (TÜBİTAK) under grant number 20AG002.

TABLE OF CONTENTS

ABSTRACT v

ÖZ vii

ACKNOWLEDGMENTS x

TABLE OF CONTENTS xi

LIST OF TABLES xiv

LIST OF FIGURES xv

LIST OF ABBREVIATIONS xviii

LIST OF SYMBOLS xx

CHAPTERS

1 INTRODUCTION 1

1.1 Climate change 1

1.2 Renewable Energy 2

1.3 Solar Cells 4

1.3.1 Working Principles of Si Solar Cells 4

1.3.2 Types of solar cells 8

1.4 Solar Cells Characterization Parameters 11

1.5 Loss Mechanisms in c-Si Solar Cells 14

1.5.1 Resistive (Electrical) Losses 15

1.5.2 Optical Losses 16

1.5.3 Recombination Losses 17

1.6 Passivation in c-Si Solar Cells 19

1.7 Zirconia as an Electron Selective and Passivation Layer 22

1.8 Aim of This Work 24

2 THEORY 25

2.1 Contacts and Contact Resistivity (ρ_c) 26

2.1.1 Band-diagrams 26

2.1.2 Interfaces 28

2.1.3 Ohmic and Rectifying Contacts 31

2.1.4 Charge Carriers Transport 33

2.2 Cox and Strack Method (CSM) 33

3 DEPOSITION AND CHARACTERIZATION OF ZIRCONIA THIN FILMS 37

3.1 Solution Processing 37

3.2 Atomic layer deposition (ALD) 41

3.3 Thermal Evaporation 43

3.3.1 Experimental procedure 43

3.3.2 Results and discussion 45

3.4 Electron Beam (E-beam) 46

3.4.1 Background 46

3.4.2 Results and discussion 47

3.5 Contact Resistivity Measurements 51

4 SOLAR CELL IMPLEMENTATION 57

4.1 n-Si in PV industry 57

4.2 Fabrication of a ZrO_x-Passivated n-Si Solar Cell 58

4.3 Performance of the solar cell 60

4.3.1 Electrical Characterization 60

4.3.2 Optical Characterization 62

5 CONCLUSIONS AND FUTURE RECOMMENDATIONS 65

5.1 Conclusions 65

5.2 Recommendations 66

REFERENCES 67

A. Appendix A 85

LIST OF TABLES

TABLES

Table 1. Comparison between efficiencies of different types of single-junction terrestrial solar cells along their relative manufacturers as of 2021. Values taken under AM 1.5G at 25 °C. Adapted from [33]..10

Table 2. Summary of the solution processing attempts for ZrO_x deposition..........40

Table 3. Design of experiment for the ALD of ZrO_2 on c-Si using TDMZr..........42

Table 4. Different parameters for different samples for ZrO_x films and their relative lifetime and iV_{OC} measurements. 46

Table 5. The shadow mask's contacts diameters, B values and R_S. 53

Table 6. Each contact with its relative total resistance R_T obtained, $R_T – R_S$ and the reciprocal of the contact's area. 54

LIST OF FIGURES

FIGURES

Figure 1. Global CO_2 emissions from fossil fuels and land use change [8]. 2
Figure 2. Share of primary energy that comes from solar energy [11]. 3
Figure 3. 3D schematic illustration of a basic solar cell under illumination............ 5
Figure 4. The AM 1.5G solar spectrum and the portion absorbed by c-Si [22]....... 7
Figure 5. Diagram showing PV technologies classified into generations: silicon (first), semiconductor compounds (second) and emerging materials (third) [30]. ... 9
Figure 6. The single diode electric circuit model of an operating solar cell. 12
Figure 7. Different I-V curves a) in dark, b) under illumination, and c) under strong illumination. A d) J-V curve under strong illumination showing the FF, V_{OC} and J_{SC}. 13
Figure 8. 3D schematic of a c-Si solar cell's components that contributes to the resistive losses. 15
Figure 9. Contribution of different recombination losses in a Si-based solar cell [55]. 19
Figure 10. Schematic illustration of the formation of energy bands when many Si atoms bond [109]. 27
Figure 11. A schematic illustration of the band-diagrams of a) intrinsic, b) n-type and c) p-type semiconductors. 28
Figure 12. Schematic representation of an energy band-diagram of an ideal MS interface. The two dashed black lines represents the interface. 29
Figure 13. Schematic representation of a real energy band diagram of MS. 30
Figure 14. Hypothetical I-V curves for ohmic and Schottky contacts. 32
Figure 15. Carriers transport mechanisms in MS junctions. 33
Figure 16. Schematic representation of the shadow mask used in CSM 35
Figure 17. Visible coating (at the top left edge) on a c-Si wafer by HFZ solution using spin-coating technique. 38

Figure 18. Normalized Raman analysis for the HFZ spin-coated c-Si sample a) the full spectrum and b) focused on the peaks related to ZrO_2. 38
Figure 19. TG and DTA analysis of HFZ in powder form. At 425 °C, physically attached water in HFZ is evaporated. 39
Figure 20. SEM images of BM1 a) spin-coated, b) spray-coated, and c) dip coated on c-Si. The coating parameters and temperatures are presented in Table 2. 39
Figure 21. SEM images of ZRAH coated on c-Si using spin coating technique at a) 300 μm, b) 1 mm scales for the same sample. 41
Figure 22. Schematic representation of an ALD cycle [126]. 42
Figure 23. The XPS signal for a) Zr 3d and b) O 1 obtained from characterizing ZrO_2 thin-layer that is deposited on c-Si using ALD. 43
Figure 24. a) Schematic view of the thermal evaporation setup and b) a virtually thick layer of Zr metal deposited on a c-Si substrate by thermal evaporation. 44
Figure 25. The XPS depth profiling for thermally evaporated Zr on c-Si a) as-deposited (E8) and b) annealed at 300 °C for 20 min (E9). 45
Figure 26. a) Schematic of the e-beam setup. b) 50 nm thick ZrO_x film (purple) coated using e-beam onto a c-Si substrate. 47
Figure 27. The SE fittings of a) tan (Ψ), b) cos (Δ) vs Energy and c) the final results where n and k are calculated. 48
Figure 28. The XPS core level spectra of 1 nm thick ZrOx on n-Si for a) Zr 3d and b) O 1s. 49
Figure 29. a) XPS survey scan for 1 nm thick ZrOx deposited on n-Si by e-beam and b) XPS depth profile of the 50 nm thick ZrOx coated on n-Si. 49
Figure 30. XRD result for 50 nm thick ZrO_x film coated onto glass substrate. 50
Figure 31. a) Tauc plot, b) transmittance, and c) absorbance of 50 nm thick ZrO_x film. 51
Figure 32. 3D schematics of the CSM structure are used to measure the I-V curves. 52
Figure 33. I-V curves of the n-Si / 1 nm thick ZrO_x / Al structure from a) -0.5 V to 0.5 V and b) 0 V to 0.5 V. 53

Figure 34. R_T-R_S vs the reciprocal of area for each contact. The slope of the trending-line represents the ρ_c. 54
Figure 35. Contact resistivity (ρ_c) values extracted using CSM vs the thickness of ZrO_x layer in a n-Si/Al structure. 55
Figure 36. I-V curves for Al / n-Si / Al structure. Predominated Schottky behavior is shown. 55
Figure 37. 3D schematic illustration of our ZrO_x passivated n-Si solar cell.......... 59
Figure 38. The J-V curve for 1 nm thick ZrO_x passivated n-Si solar cell with Al rear contact. 61
Figure 39. EQE of n-Si solar cell with a rear contact of 0, 1, and 5 nm ZrO_x with Al as a back metal contact.......... 63

LIST OF ABBREVIATIONS

ABBREVIATIONS

(BM1)	Bonderite M-NT-1
4PP	4-Point-Probe
ALCVD	Atomic layer chemical vapor deposition
ALD	Atomic layer deposition
AM	Air Mass
ARC	Antireflective coating
CB	Conduction band
CNL	Charge neutrality level
CO_2	Carbon dioxide
COVID19	Coronavirus disease of 2019
c-Si	Crystalline silicon
CVD	Chemical vapor deposition
DC	Direct current
DSP	Double side polished
DSSS	Dye-synthesis solar cells
Ebeam	Electron beam deposition
EHP	Electron Hole Pair
EM	Electromagnetic
FLP	Fermi-level pinning
H_2O	Hydrogen dioxide (water)
HFZ	Hexafluoro-zirconicacid
IM	Interlayer/metal
IS	Interlayer/semiconductor
MOCVD	Metal-ogranic chemical vapor deposition
MOS	Metal oxide silicon
MS	Metal/semiconductor

N_2	Nitrogen gas
n-Si	n-type crystalline silicon
OPV	Organic photovoltaics
PEDOT:PSS	Poly(3,4-ethylenedioxythiophene) polystyrene sulfonate
p-Si	p-type crystalline silicon
PVD	Physical vapor deposition
RCA	Radio Corporation of America
RF	Radio frequency sputtering
SBH	Schottky barrier height
SE	Spectroscopic ellipsometry
Si	Silicon
SiN_x	Silicon nitride
SiO_2	Silicon dioxide
SQL	Shockley-Queisser Limit
TDMZr	Tetrakis (dimethylamido) zirconium (IV)
TGA	Thermogravimetric analysis
VB	Valence band
UV	Ultraviolet
XPS	X-ray photoelectron spectroscopy
XRD	X-ray diffraction
ZRAH	Zirconium acetate hydroxide
ZrO_2	Zirconium dioxide
ZrO_x	Zirconium oxide

LIST OF SYMBOLS

SYMBOLS

C_{ox}	Capacitance of an oxide
E_0	Vacuum energy level
E_C	Conduction band minimum
E_F	Fermi-level
E_V	Valence band maximum
I	Electric current
I_0	Reverse saturation current
I_L	Photo-generated current
K	Kelvin
k	Boltzmann constant
^{o}C	Degree Celsius
R_{SH}	Sheet resistance
R_{Series}	Series resistance
V	Electric voltage
ε_0	Permittivity of air
ε_{ox}	Permittivity of an oxide
κ_{ox}	Dielectric constant of the oxide
ρ_c	Contact resistivity
Φ	Work function

CHAPTER 1

INTRODUCTION

1.1 Climate change

Our planet is experiencing alterations in its climatological conditions, which is referred to as climate change [1]. Earth receives solar radiation, and then it releases some heat back, in the form of infrared waves, while cooling down. Methane, nitrous oxide, and carbon dioxide (CO_2), among other gases, reflect this infrared radiation back to Earth. These gases are called greenhouse gases. CO_2 is the most produced gas with its concentration in the atmosphere increased by over 40% since the 1800s [2]. The other greenhouse gases' concentrations have also increased drastically. This increase is believed to be a result of the Industrial Revolution [3]. This puts human lives and existence in danger [4] as it has resulted in different climatical events like heat waves, droughts, the rise of sea level, and, most crucially, a rise in the average temperature of the planet by 0.85 °C since 1880 [2]. Global warming is the term used to describe such a temperature increase. In 2010, the amount of money spent on damage repair worldwide that resulted from global warming was estimated to be billions of dollars [5].

The annual global requirement for energy in 2015 is estimated to increase by more than 50% by the year 2040 [6]. The primary factor that could handle this rising demand for energy will be a robust and sustained economic expansion in all countries across the globe [6]. Greenhouse gas emissions are attributed directly to the production of energy through fossil fuels, as shown in Figure 1. Besides being limited, it is getting harder to extract fossil fuels from their sources. This pushes companies and governments to take more risks, as was seen in the Gulf of Mexico

in 2010 [7]. If humanity continues to use hydrocarbon-based energy sources at the same rate, these sources will not only eventually run out but will have irreversible adverse environmental effects, such as global warming, that could lead to an uninhabitable planet. Therefore, it is necessary to benefit from different energy sources in order to stop or at least slow down global warming and climate change.

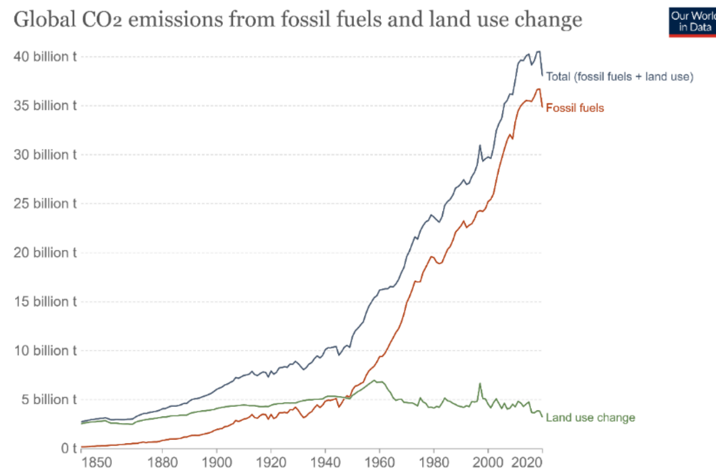

Figure 1. Global CO_2 emissions from fossil fuels and land use change [8].

1.2 Renewable Energy

Energy is defined as the quantitative property that must be transferred to a body to perform work on it or to raise its temperature. Renewable energy can be defined as the energy that comes from a source that generates energy with a rate faster than its consumption rate. Renewable energy refers to virtually and practically inexhaustible energy resources such as sunlight, wind, flowing water, and many other earth-related sources, e.g., Earth's internal heat and biomass, such as energy wastes. The essentially needed types of energies such as electricity, heat, and fuels can all be produced from these self-renewing energy sources. Harnessing solar power is no longer the talk of the future as humans have strived to capture and use sunlight for centuries [9]. As of 2021, renewables contribute to over 13% of the energy produced worldwide [10]. In 2019, 1.6% of the world's energy

generated came from solar power, with Chile leading this trend as 6% of its energy was provided by solar energy [11] as shown in Figure 2.

Our modern society would not exist without electricity, which we access to the power grid and ultimately contribute to our quality of life. Human civilization relies heavily on fossil fuels to generate electric energy, with over 10,000-terawatt hour (TWh) of electricity generated using coal in 2021 only [12]. Currently, renewables generate more than 28% of all electricity produced globally, with Brazil having almost 79% of its electricity produced by renewables, followed by Sweden with 67% [13].

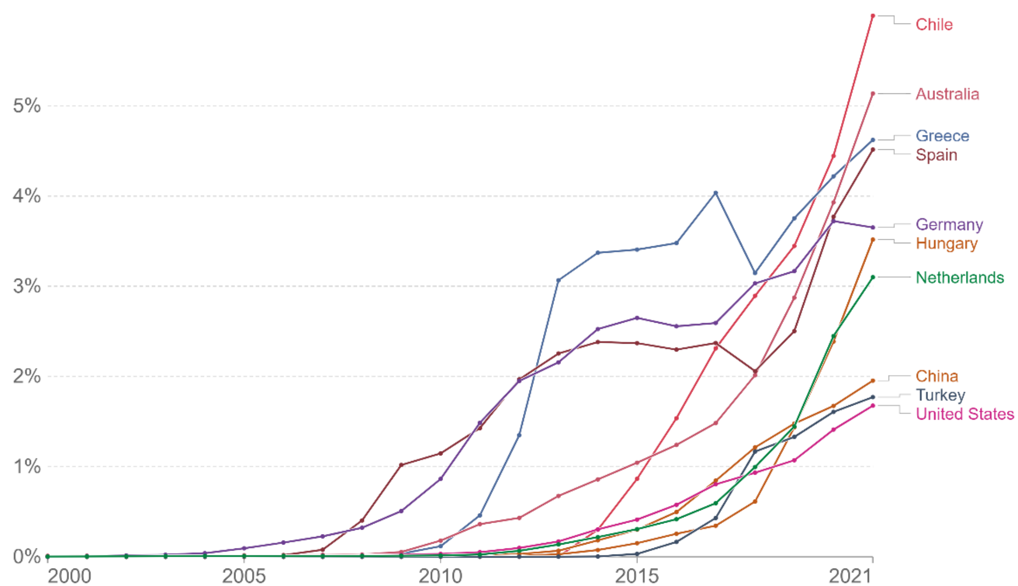

Figure 2. Share of primary energy that comes from solar energy [11].

Earth, in one hour, receives 4.3×10^{20} J from the sun, which is more than all the energy needed by humankind in one year (4.1×10^{20} J) [14]. While harvesting all the energy sent by the sun is practically impossible, these numbers give an idea of the potential that lies in solar power. The sun is arguably the most fundamental energy source known to mankind. Fossil fuels could be viewed as a product of millions of years of solar energy stored in the form of chemical energy. Moreover, wind is the result of temperature differences in the atmosphere, which occur owing to solar irradiation. Ocean waves are generated by winds. Clouds and rains are also

formed from evaporation which occurs due to sunlight. With that in mind, utilizing solar energy is indispensable for the future of humanity. Solar cells are currently the main way of harnessing solar energy.

1.3 Solar Cells

A solar cell could be defined as a device that converts light into electricity using the photoelectric effect. They are primarily made up of semiconductors. In 1883, Charles Fritts made the first solar cell [15]. Only by the 1950s, extensive research on solar cells took a serious route [16]. In the following sections, the principles of semiconductors and solar cells, as well as the types of solar cells, are discussed.

1.3.1 Working Principles of Si Solar Cells

In its essence, a solar cell is a pn junction that absorbs electromagnetic (EM) waves and produces an electric current. A semiconductor, metal contacts, and an antireflective coating (ARC) are the three main components of a solar cell. Electron-hole pairs (EHP) are generated when a photon is absorbed by the semiconductor layer, while the ARC helps keep the incident light from reflecting. Extraction of the light-generated charge carriers is done through the metal contacts. This is schematically illustrated in Figure 3.

Light-induced EHPs are generated because when a photon hits the solar cell surface, it excites an electron giving it enough energy to make it move to the conduction band (CB), leaving its hole counterpart in the valency band (VB), i.e., making the electrons and the holes free to move. Put simply, CB and VB are made of energy levels (energy values) that electrons and holes can occupy (have). The effective density of states of the VB and CB depend mainly on the material. For silicon (Si), at room temperature, the effective density of states of both N_v (VB)

and N_c (CB) are in the order of ~ 10^{19} cm^{-3}. These values are theoretically calculated in literature [17].

In an operating solar cell, the photogenerated EHPs can be referred to as minority charge carriers under low-level injection condition. To generate current, the minority charge carriers must cross the pn junction in the solar cell structure without recombining with one another. If they are extracted before they recombine, an electric current is generated. The reasons and solutions for the EHP recombination phenomenon, along with other losses in solar cells, are discussed later in this chapter.

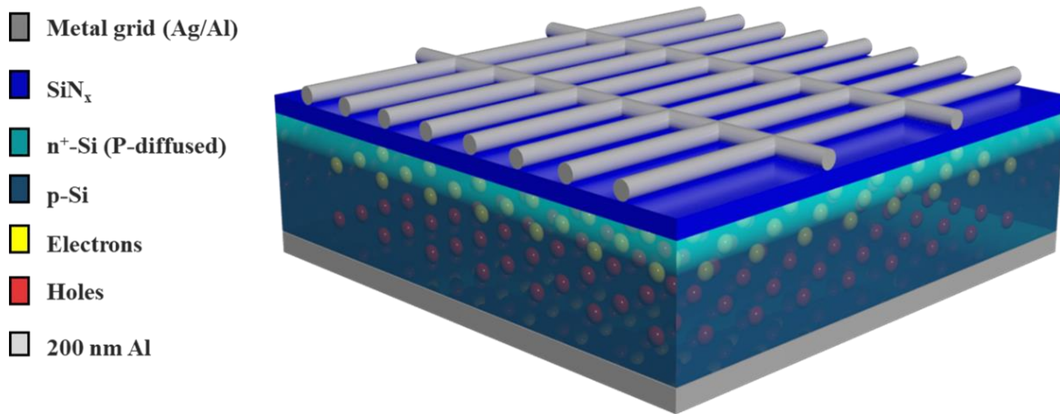

Figure 3. 3D schematic illustration of a basic solar cell under illumination.

The sun's surface behaves (roughly) as a blackbody with a temperature of 6000 Kelvin (K), which gives EM radiation. In total, 77% of the sunlight coming from outside the atmosphere reaches the surface of Earth. The losses are due to the reflection and absorption of the sunlight by the atmosphere (e.g., H_2O, O_2, O_3, CO_2) and the scattering that happens [18], particularly, in the blue wavelengths of the spectrum. Scattering of light in the atmosphere occurs due to Rayleigh scattering (scattering without a change in wavelength), which gives the sky its blue color. These losses make the intensity (i.e., irradiance) of sunlight to depend on the thickness of the atmosphere. This is known as Air Mass (AM).

$$AM = \frac{Length\ of\ the\ path\ traveled\ by\ light}{vertical\ depth\ of\ the\ atmosphere} = \frac{1}{\cos\theta}$$

Eq. 1

The Zenith angle (θ) is the angle between the sun's rays from the perpendicular to the Earth's surface. The standard spectrum at the Earth's surface is called AM 1.5G, where G stands for global and includes direct and diffuse radiation. AM 1.5D refers to direct radiation only. AM1.5 corresponds to a θ of 48.2°, which is internationally used in testing solar cells [19]. The intensity of AM 1.5G radiation is calculated to be 970 W/m^2 which is approximated to 1 kW/m^2 for convenience [20].

Silicon has a band gap of 1.12 eV, which allows it to only absorb radiation below 1100 nm. This is calculated in Eq. 2. Figure 4 vividly shows the portion of the solar spectrum that can be absorbed and used by c-Si solar cells with reference to the entire solar spectrum that reaches Earth. As discussed in Section 1.3.1, the incident photon must have energy more than or equal to the band gap of the semiconductor to be absorbed and to create an EHP. In Si, photons with energies less than 1.12 eV (which means wavelengths larger than 1107 nm from $\lambda = hc/E_g$) cannot be absorbed. Similarly, photons with wavelengths equal to and lower than approx. 300 nm will mainly be reflected by Si surfaces, which explains the blue color of c-Si solar cells. The solar spectrum that reaches Earth's sea level, and thus solar plants, is between ca. 300 nm and up to more than 2500 nm. In 1960, a study was made regarding the exposure of c-Si solar cells to photons with higher energies, such as X-rays and γ-rays. It was reported that a rise in the temperature of the solar cell occurred, which led to a considerable decrease in its efficiency [21]. This is to say that prolonged exposure to low wavelengths of the spectrum might negatively affect the solar cell's performance. Note that Si reflectivity increases to more than 70% with wavelengths ranging below 300 nm.

$$\lambda = \frac{hc}{E} = \frac{1240\ eV * nm}{1.12\ eV} = 1100\ nm$$

Eq. 2

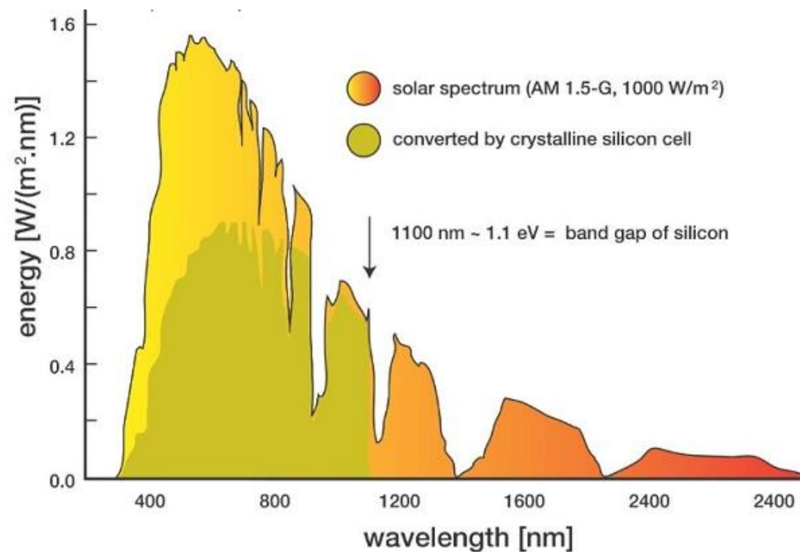

Figure 4. The AM 1.5G solar spectrum and the portion absorbed by c-Si [22].

As of 2022, single junction c-Si solar cell modules have achieved an efficiency of 24.4%, while Kaneka Co. claimed a c-Si hetero-structure (HJ) solar cell with interdigitated back contacts (IBC) reaching 26.3% [23]. Table 1 lists the highest efficiencies of c-Si solar cells. They have a typical efficiency of 21%, making them the most cost-effective - high-performing solar cells in today's market. From the processing of raw silica sand to a fully functioning solar cell is a reliable and well-studied process.

Si solar cells cannot absorb or utilize all the solar energy that reaches them, as shown in Figure 4. This fact is taken into account by the Shockley-Queisser Limit (SQL) calculations. SQL states that the highest possible theoretical efficiency of a single pn-junction Si-based solar cell is about 30% [24].

There are other types of solar cells that have higher efficiencies. The highest solar cell was reported to have an efficiency of 47% [25] in 2021. These cells make use of multi-junctions rather than a single junction. An example of a multijunction solar cell is the AlGaInP/AlGaAs/GaAs/GaInAs structure [26]. They also use lenses to concentrate the light falling on them. These cells are currently expensive. They are used in satellites and space exploration. The theoretical efficiency limit for a 5-junction solar cell under a concentrator is about 65% [27].

1.3.2 Types of solar cells

One of the ways to categorize solar cells is by assigning different types to different generations. There are other forms of classifications of solar cells. The classification of these generations is mainly based on the complexity of manufacturing, the absorption capacity, the band gap, and the crystallinity of the materials used. Each generation is briefly introduced in this section. Figure 5 shows the classifications of distinct types of solar cells according to generations.

The 1st generation solar cells are the ones predominately made from silicon, whether it is monocrystalline or polycrystalline. This type of solar cell, to this day, dominates the photovoltaic (PV) market [28]. The main reason could be attributed to its stability, reliability, and longevity in its working environment. With Si being the second most abundant element on earth, prices of Si are relatively low. Among the three generations, the second generation of solar cells is reported to have the lowest efficiency and manufacturing cost. This generation is also referred to as thin film solar cells. Cadmium telluride (CdTe) is the most used material in that category and the second most used material is copper – indium - gallium – selenide (CIGS). Amorphous silicon (a-Si) is in that class of solar cells as well.

The third generation is seen as the most developed generation and has the potential to exceed the SQL as it consists of solar cells with more than one band gap material in their structures. New and innovative work is usually done on that generation. Some of these innovations are organic photovoltaics (OPV) and polymer solar cells, where the absorption and charge transport occurs in a molecule or in a polymer [29]; dye-synthesized solar cells (DSSS) which are based on a photo-electro-chemical system where a semiconductor material based on molecular sensitizers, is placed between a photo-anode and an electrolyte; perovskites solar cells are made from materials exhibiting a perovskite crystal structure such as hybrid organic-inorganic lead or tin halide-based material, as the primary photon-capturing material.

Other technologies are being utilized in that generation, including quantum dot sensitized solar cells (QDSSC), intermediate band gap solar cells, hot carrier solar cells, and more. The multi-junction solar cells based on the III-V (e.g., GaAs) materials, which are usually deposited on germanium (Ge), have the highest efficiency as of today.

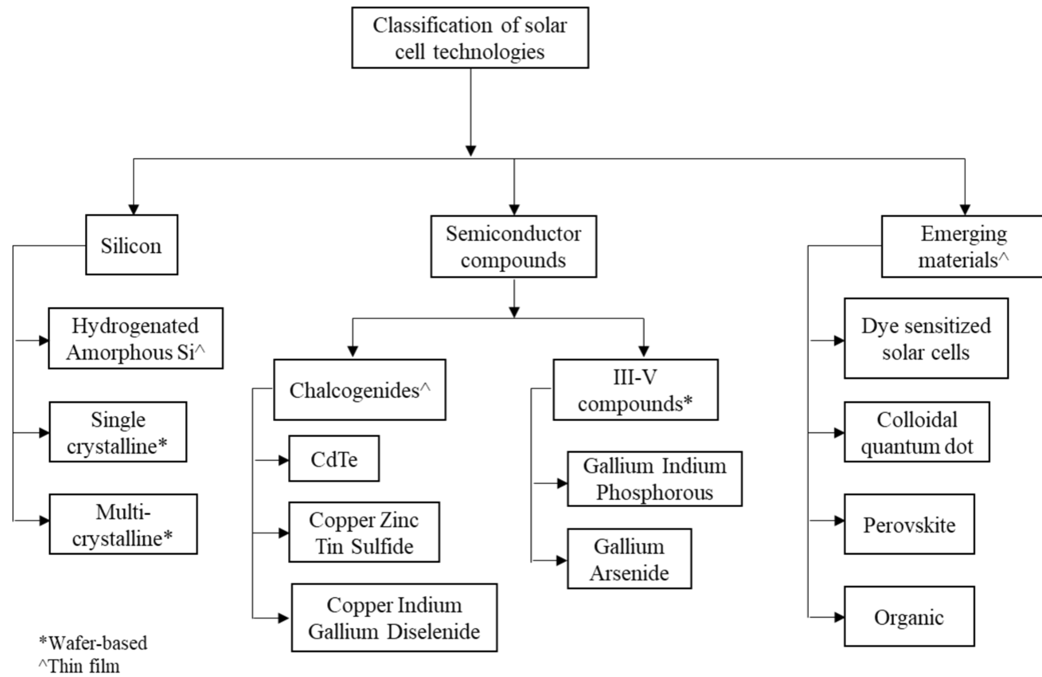

Figure 5. Diagram showing PV technologies classified into generations: silicon (first), semiconductor compounds (second) and emerging materials (third) [30].

Table 1 lists several types of solar cells and their reported efficiencies with an uncertainty between ± 0.2 and ± 0.6. It is worth mentioning that solar cell efficiency limits calculations, and theories, other than SQL, have been developed over the years. Theoretical calculations showed that a solar cell could reach at most 85.4% efficiency under concentrated sunlight [31]. Honsberg et al. argue that there is room for improvement in the current design of multi-junction PVs by making use of the nanostructured form of the same materials currently used. They also noted that more junctions could be added to the current multijunction structures. The mentioned theoretical limits were verified by De Vos et al. in 1981 [32].

Table 1. Comparison between efficiencies of different types of single-junction terrestrial solar cells along their relative manufacturers as of 2021. Values taken under AM 1.5G at 25 °C. Adapted from [33].

Classification	*Efficiency (%)*	*Description*	*Ref.*
		Silicon	
Si (crystalline cell)	26.7	Kaneka, n-Si rear IBC	[23]
Si (multicrystalline cell)	24.4	Jinko Solar, n-Si	
Si (thin transfer submodule)	21.2	Solexel (35 µm thick)	[34]
Si (thin film minimodule)	10.5	CSG solar (<2 µm on glass)	[35]
		III-V cells	
GaAs (thin film cell)	29.1	Alta devices	[36]
GaAs (multicrystalline)	18.4	RTI, Ge substrate	[37]
InP (crystalline cell)	24.2	NREL	[37]
		Thin film chalcogenide	
CIGS (cell)	23.35	Solar frontier	[38]
CdTe (cell)	21	First solar, on glass	[39]
CZTS (cell)	10.0	UNSW	[40]
		Amorphous/microcrystalline	
Si (amorphous cell)	10.2	AIST	[41]
Si (microcrystalline cell)	11.9	AIST	[42]
		Perovskite	
Perovskite (cell)	22.6	ANU	[43]
Perovskite (minimodule)	20.1	UtmoLight, 12 cells	[44]
		Dye sensitized	
Dye (cell)	11.9	Sharp	[45]
Dye (minimodule)	10.7	Sharp, 7 serial cells	[36]
Dye (submodule)	8.8	Sharp, 26 serial cells	[36]
		Organic	
Organic (cell)	15.2	Fraunhofer ISE	
Organic (minimodule)	13.6	WAYS/Nanobit/NCU (16 cells)	

1.4 Solar Cells Characterization Parameters

The performance of a PV device could be evaluated according to two main categories: electrical and optical parameters. The electrical parameter is addressed, followed by the optical parameter.

When a voltage is applied to a conductor, electric current is bound to pass through it, usually, with a linear relation with the resistance of the conductor being the linearity constant. However, in semiconductors and insulators, the relation between current and voltage tends to be more complicated. The relation between current and voltage (I-V) differs depending on the type of junction. Since a solar cell is, in essence, a pn junction, its I-V behavior, in the dark, could be modeled by Eq. 3, which is referred to as the *diode current,* I_D.

$$I = I_D = I_0 \left(e^{qV/nkT} - 1 \right)$$

Eq. 3

, where k is the Boltzmann constant, T is the absolute temperature, n is the ideality factor, q is the unit of elementary charge, and I_0 is the *reverse saturation current*. The derivation of the equation and what exactly is I_0 can be found in the referenced textbook [17]. The ideality factor, n, is usually taken to be 1 in solar cells as they are quite large compared to conventional diodes. In some textbooks, the term kT/q is referred to as the thermal voltage, V_T, which is about 0.0259 V at 25 °C and is used in Eq. 3. By subtracting the right side of Eq. 3 from the *photogenerated current*, I_L, the I-V behavior of an operating solar cell under illumination can be deduced as shown in Eq. 4.

$$I = I_L - I_D = I_L - I_0 \left(e^{qV/nkT} - 1 \right)$$

Eq. 4

There are more accurate ways to model the electrical behavior of an operating solar cell. The single diode model expresses an operating solar cell in terms of an electric

circuit, as illustrated in Figure 6. It is the most widely used model due to its simplicity and accuracy. The shunt resistance (R_{Shunt}) and the series resistance R_{Series} are two forms of losses, where R_{Shunt} represents any alternative way of current to flow through, and R_{Series} is responsible for any drop of voltage while the current is flowing. R_{Series} is discussed in section 1.5.1. Ideally, R_{Shunt} should be as large as possible, while R_{Series} should be as close to zero as possible. Taking R_{Shunt} and R_{Series} into account, another term of current loss, shunt current, I_{Shunt} must be added to Eq. 4, which is shown in Eq. 5.

$$\boldsymbol{I} = I_L - I_D - I_{Shunt} = I_L - I_0\left[e^{\left[\frac{q(V+IR_{Series})}{nkT}\right]} - 1\right] - \frac{V + IR_{Series}}{R_{Shunt}}$$

Eq. 5

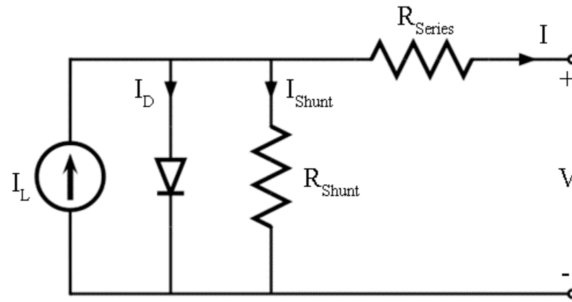

Figure 6. The single diode electric circuit model of an operating solar cell.

Another more realistic way of modeling an operating solar cell is the double-diode model, where other forms of losses, i.e., recombination losses, are considered.

To eliminate the effect of size on the performance of a solar cell, the current density (J) concept is used instead of current (I). J is the amount of current that passes through a unit area. Current is expressed in milliamperes (mA), while the area is expressed in centimeter square (cm^2), making J expressed in mA/cm^2. The current density versus voltage (J-V curves) graphs are of utmost importance to assess the solar cell's diode and contacts electrical behavior.

In dark, minority charge carriers cannot overcome the metal-semiconductor (MS) boundary in a solar cell to contribute to the current. Under illumination, the

minority charge carrier concentration increases exponentially, making it easier to cross the boundary and contribute to the current flow. Figure 7 (a), (b), and (c) show the I-V curve behaviors wherein light is absent, present, and strongly present, respectively. Figure 7 (d) shows a J-V curve (flipped for convenience) for a solar cell under strong illumination. It also shows essential parameters in characterizing an operating solar cell, which are: the short circuit current (I_{SC}), which is the current produced when the circuit has zero voltage, the open circuit voltage (V_{OC}), is which is voltage under open circuit conditions, and the fill factor (FF) which is shown as the purple shaded area in Figure 7 (d). Recall that, in the dark, the solar cell behaves (electrically) like a diode; the relationship between I_{SC} and V_{OC} can be seen in the diode equation. FF is the ratio of $\frac{\boldsymbol{V_{MP}\,I_{MP}}}{\boldsymbol{V_{OC}\,I_{SC}}}$ where I_{MP} and V_{MP} are the current and the voltage values, respectively, at which the maximum power that can be extracted from the solar cell occurs. The V_{OC} could be derived by setting Eq. 4 to zero, which results in Eq. 6. To find I_{SC}, the voltage term in Eq. 4 is set to zero. This results in I_{SC} equals IL, where I_{SC} is the largest current that could be drawn from the solar cell.

$$V_{OC} = {}^{nkT}/_{q}\left(\ln\frac{I_0}{I_L} + 1\right)$$

Eq. 6

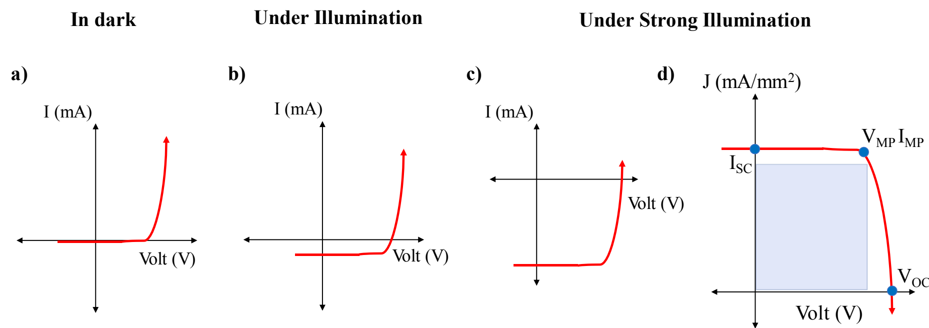

Figure 7. Different I-V curves a) in dark, b) under illumination, and c) under strong illumination. A d) J-V curve under strong illumination showing the FF, V_{OC} and J_{SC}.

External quantum efficiency (EQE) is an optical characterization parameter defined as the ratio of the number of charge carriers collected by the solar cell to the number of incident photons. At best, one EHP will be generated per each incident photon, which means that EQE cannot exceed 1.

Researchers at Wuppertal University were able to achieve an EQE of 0.98 for perovskite solar cells [46]. Other researchers [47], in the quantum dot solar cells field, investigate the so-called multiple exciton generation (MEG), which contrary to common belief, claims that a single photon could be responsible for the generation of more than one exciton (i.e., EHP in the same vicinity). Nevertheless, this is yet to happen in c-Si solar cells. Light bias (LB) is a mode used in some EQE measurements to account for the defects on the Si surface. It follows the exact measurement process described in the previous paragraph while only shining light with a specified intensity on the whole solar cell.

The power conversion efficiency (PCE) of a solar cell is the most common and convenient way to assess the behavior of a solar cell. It is defined as the ratio of the power that can be converted from the incident light to the actual power converted and extracted from the cell. PCE is reported in percentage form and assigned the small Greek Eta symbol (η).

$$\eta = \frac{P_{out}}{P_{in}} = \frac{I_{MP} \times V_{MP}}{P_{in}} = \frac{V_{OC} \times J_{SC} \times FF}{P_{in}}$$

Eq. 7

1.5 Loss Mechanisms in c-Si Solar Cells

Losses in a solar cell could be divided into three main categories, that are optical losses, electrical losses, and losses due to recombination [24]. Some researchers classify the losses into only optical and electrical since the former addresses the photons capture process while the latter addresses the charge carriers

capture process, thus combining the recombination losses under the electrical losses category.

Other forms of losses, such as temperature, design, and fabrication defects, affect the efficiency of the solar cell. For example, for every 1 K rise in a c-Si solar cell's temperature, its efficiency drops by 0.45-0.6%, as well as its fill factor (FF) decreases by 0.2% [48]. More forms of losses happen in c-Si solar cells; however, the ones mentioned above are the most contributing. Electrical and optical forms of losses are explained in the following sections.

1.5.1 Resistive (Electrical) Losses

The electrical losses could be reduced by reducing the series resistance from the contacts, top grid, base, and the emitter's sheet resistivity, as shown in Figure 8. For the emitter, the precise thickness and resistivity are hard to measure. However, the ratio of resistivity to thickness (known as sheet resistance, R_{SH}) of a uniformly doped emitter layer could easily be measured. It yields results in ohm/sq units. The emitter and the top grid contribute the most to the parasitic resistive losses in a solar cell. The top grid, which consists of busbars and metal fingers, must be optimized in design so that minimum losses occur when transferring the current through them.

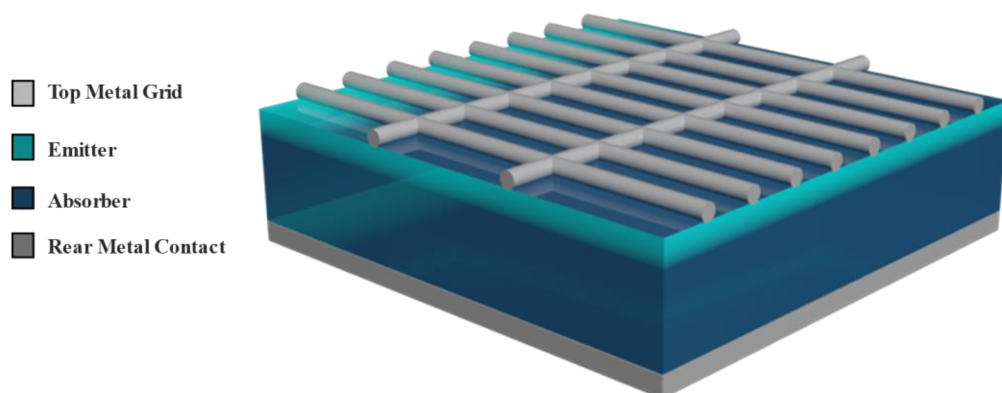

Figure 8. 3D schematic of a c-Si solar cell's components that contributes to the resistive losses.

1.5.2 Optical Losses

Si surface reflects approximately 30-40% of the visible sunlight. This value could be calculated from the refractive index of silicon, as shown in Eq. 8. Refractive index of Si (n_{Si}) depends on the wavelength of the incident light, but it typically falls between 3.5 and 4.5. This reflection contributes remarkably to the optical losses in a Si-based solar cell.

$$R = \frac{(n_0 - n_{Si})^2}{(n_0 + n_0)^2} = \frac{(1 - 3.5)^2}{(1 + 3.5)^2} = 30\%$$

Eq. 8

Below are some of the methods used to minimize the optical losses. The main idea is to decrease the Si reflectance and increase its absorbance.

- Applying ARC. In Si solar cells, the ARC is usually silicon nitride (SiN_x). The ARC plays a crucial role in minimizing the optical losses as it reflects about 7% of the incident light rays. This is due to its small refractive index, which lies between 1.75 to 2.25 depending on the fabrication method [49].
- Applying surface texturing to trap the light by multiple reflections along the surface. This is done, in Si wafers, by potassium hydroxide (KOH) treatment discussed in Chapter 4.
- Increasing the material's thickness. This could be tricky as thick wafers are expensive. However, the thicker the material is, the higher fraction of incident light (I_0) absorbed by the material as depicted by $I_x = I_0 e^{(-\alpha x)}$, where x is the distance traveled by the incident light with intensity I_0 in the material and α is the *absorption coefficient*. α is a function of both the wavelength of the incident light and a material's property [17]. α is easy to measure but difficult to calculate. For instance, in a Si wafer of a thickness larger than 10 mm, almost all light with energy above the band gap is absorbed. Thus, engineers and researchers are continuously trying to optimize the bulk material, so it is mechanically thin and optically thick.

- Using Lambertian Rear Reflector. This reflects any light that reaches the rear end of the cell with a random angle of reflection. This increases the path length of light inside the semiconductor by a factor of $4n^2$, n being the refractive index of the material (e.g., semiconductor) [50].

It is worth mentioning that the metal grid (fingers and busbars) also contributes to the reflection of the incident light on a solar cell. This shading effect has a detrimental impact on the short circuit current (I_{SC}) of the solar cell. A widely spaced grid provides a better light capture but a higher resistive loss. Thus, optically transparent conductors can be applied to light reflection problems, but their electrical conductivity is much lower than metals, and they tend to absorb light [51].

1.5.3 Recombination Losses

When light is absorbed by the c-Si in a solar cell, EHPs are generated everywhere in the bulk. However, only the charge carriers within a diffusion length (L_D) to the pn junction contribute to the photogenerated current. This is because the charge carriers must cross the junction to be extracted. The electric field created by the fixed ions in the depletion region (the junction) is the primary driving force for the minority charge carriers (photogenerated) to cross the junction. The problem occurs when these charge carriers recombine. This EHPs recombination means current loss.

For a semiconductor, at a given temperature (non-zero K), in the dark, there is an equilibrium state between the rate of recombination and the rate of generation of EHPs. Under illumination, more EHPs get generated. Those photogenerated EHPs are considered “excess” EHPs. For the system to reach thermodynamic equilibrium again in the semiconductor, the rate of EHPs recombination increases.

It is essential to differentiate between surface recombination and bulk recombination. The reasons for bulk recombination could be classified into

extrinsic and intrinsic. Auger recombination happens when, for instance, an excited electron in the CB releases energy to move back to the VB; hence, it increases with increasing the charge carriers density i.e., doping concentration. The energy released is absorbed by either another electron in the CB or a hole in the VB. It happens in heavily doped Si, as Si is an indirect band gap semiconductor; thus, momentum transfer is possible, unlike direct band gap material where mostly radiative recombination occurs as only the emission of a photon is required for charge carriers to move to a lower energy state. Radiative recombination happens when an excited electron releases a photon. This is not a concern for Si because it requires the presence (emission) of a phonon (to account for the momentum transfer) for an electron to move from VB to CB. Auger and radiative recombination are intrinsic recombination mechanisms. Shockley-Read-Hall (SRH) recombination took its name when Shockley and Read [52] developed a statistical model that was later confirmed by Hall [53] to describe the recombination rate of bulk discontinuities such as impurities, dislocations, and vacancies. These crystallographic defects create energy levels in the band gap of the semiconductor, allowing charge carriers to use them as mediators when moving from CB to VB. SRH is an extrinsic recombination mechanism.

For surface recombination, the focus of the present work, dangling bonds, from unsaturated bonds at the surface of cleaved c-Si, act as high-energy sites that facilitate recombination of EHPs. The typical density of dangling bonds of a cleaved c-Si is in the order of $10^{14}/cm^2$ [54].
Some of the known methods to solve surface recombination issues include:

1. Increase the doping concentration in the semiconductor.
2. Increase the diffusion length of the charge carriers.
3. Passivate the common recombination spots.

The contribution of different recombination mechanisms on c-Si solar cells in Figure 9 shows that rear surface recombination has the highest share. In the next section, a discussion regarding passivation to reduce recombination is present.

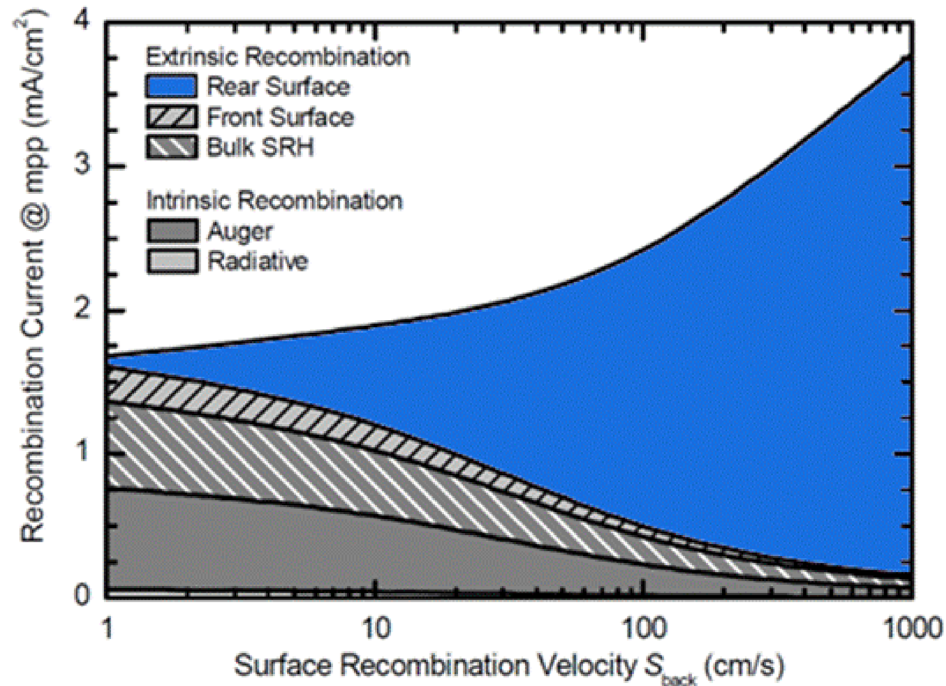

Figure 9. Contribution of different recombination losses in a Si-based solar cell [55].

1.6 Passivation in c-Si Solar Cells

For reasons meticulously discussed in Chapter 2, when specific materials (e.g., transition metal oxides, TMOs) are placed between a metal and a semiconductor (MS), the recombination rate of EHP decreases. They act as a "passivating" layer.

To passivate is to suppress. In the solar cell context, it refers to making the surface of a bulk semiconductor inert. Another important concept that could be associated with passivation is the carrier-selective property of some materials. As the name implies, this is when a material prevents a specific type of charge carrier while allowing another to pass through it. A passivating material is not necessarily a carrier-selective material (and vice versa). Indeed, some materials perfectly passivate but prevent the passage of all charge carriers [56]. Passivation could be classified into physical passivation and chemical passivation.

Chemical passivation occurs when a passivating layer saturates the dangling bonds of the surface of c-Si which prevents EHP from using the high energy sites as a recombination place [57]–[59]. Physical passivation is when a passivating layer has fixed charged particles, like ions or oxides, in its structure that repels unwanted charge carriers. In the case of SiN_x, positively charged holes are repelled by the positive charges present in the SiN_x. These positive charges create an electric field that repels holes and attracts electrons [60], thus being an "electron selective layer". SiN_x is one of the leading materials currently used in the PV industry as it provides a low surface recombination velocity (SRV) of about 3.2 cm/s [61]. Before mentioning the materials used as interlayers (passivating and/or charge carriers-selective) in solar cells, it is worth mentioning that heavily doping the rear side of the absorber semiconductor with the same dopant atoms is proven to reduce the recombination at the MS interface. This is discussed further in Chapter 4.

Other materials, such as aluminum oxide (Al_2O_3), are used as interlayers in c-Si solar cells. They are typically deposited through atomic layer deposition (ALD) [62]–[64] and by spatial ALD [65]. Al_2O_3 stands out as a passivating material and is widely used in industry due to its high amount of negative fixed charges in its structure. When it is compared with SiN_x and silicon dioxide (SiO_2), Al_2O_3 shows greater stability under ultraviolet (UV) exposure [66]. Al_2O_3 is used to passivate p-type c-Si (p-Si) based solar cells, while SiN_x and SiO_2 work best for n-type c-Si (n-Si). Other methods make use of amorphous Si (a-Si) and SiO_2 combined in a double-layer structure to act as a passivating material [67]–[70]. A combination of Al_2O_3 and SiN_x was reported to give a similar passivation behavior in a process given the name Alneal [71].

Whether a material is electron-selective or hole-selective depends on its work function (Φ), which affects its band alignment with the semiconductor with which it is in contact. Some oxide-based materials provide carrier-selective properties as well as passivation properties. In the case of c-Si, vanadium oxide (VO_x) acts as a hole-selective layer while providing a low contact resistivity (ρ_c) of 95 $m\Omega.cm^2$ [72]. Other oxide-based materials such as titanium dioxide (TiO_2) [73], tantalum

oxide (TaO_x) [74], niobium oxide (Nb_2O_5) [75], and nitride-based materials such as TaN_x [76], and TiN [77] were reported to act as electron-selective contacts for c-Si solar cells. Alkali and alkaline earth metals and their salts were also reported to act as electron-selective layers such as Mg [78], MgF_2 [79], and, of course, one of the most prominent interlayers, lithium fluoride (LiF) [80]. LiF_x acts significantly well as an electron-selective layer; however, it has poor passivating properties, which results in a relatively high EHP recombination rate at the contacts [81].

With regards to hole-selective contacts, molybdenum oxide (MoO_x) [82] is among the most prospected materials used in c-Si solar cells due to its high performance. It is reported that MoO_x deposited by ALD tends to be less efficient (lower Φ) than the thermally evaporated MoO_x [83], [84]. Tungsten oxide (WO_x) is also reported to act as a hole-selective layer in c-Si [85]. Not only metals and metal oxides but also polymers are used as interlayers in c-Si solar cells. Poly(3,4-ethylene dioxythiophene) polystyrene sulfonate (PEDOT:PSS) showed promising results when deposited onto c-Si solar cells. It has been reported to act as a hole-selective layer [86], [87]. However, polymers tend to have questionable stability under operating conditions.

Each of the materials mentioned above has at least one issue regarding them. One of the main issues facing most of the mentioned passivating layers is their deposition techniques. Most of them are deposited through ALD (e.g., Al_2O_3 and VO_x), which is a slow and expensive process. Others are not stable under prolonged exposure to specific wavelengths (e.g., SiN_x). Some are expensive (e.g., TaO_x), while others act well as a passivating layer but block all charge carriers, which is challenging and requires extra steps like laser openings. Other materials perform great as a carrier selective layer; however, their passivation properties are inadequate (e.g., LiF_x).

SiO_2 is arguably the best passivating material for c-Si [88]. Nevertheless, SiO_2 has shortcomings as the current microelectronics market is heading fast towards miniaturizing metal-oxide-semiconductor (MOS) devices. The lower its thickness

(~ 4 nm or less), the more the MOS structure is susceptible to electrical breakdowns and more tunneling of electrons through the SiO_2, as Baklanov et al. argued [89]. It also becomes more challenging to accurately control the SiO_2 growth at low thicknesses. Zirconium dioxide's (ZrO_2) carrier-selectivity and passivation properties are investigated in the following section.

1.7 Zirconia as an Electron Selective and Passivation Layer

ZrO_2 is an electron-selective material [90]–[92]. Wan et al. [93] reported that it has excellent passivation properties. They deposited 20 nm of ZrO_2 on c-Si and measured the lifetime of EHPs (i.e., for how long do EHPs stay apart). They reported up to 1.1 milliseconds lifetime, which is considerably high.

A crucial parameter in dielectrics is called capacitance (C_{ox}). In this case, the dielectric is an oxide-based material. C_{ox} is defined as:

$$C_{ox} = \frac{\kappa_{ox} * A_{ox}}{t_{ox}} * \varepsilon_0$$

Eq. 9

κ_{ox} is the dielectric constant of the oxide, which is a material property, ε_{ox} is the permittivity of free space, and A_{ox} and t_{ox} are the area and the thickness of the oxide layer, respectively. The higher C_{ox} is, the better its passivation properties, typically. Examining Eq. 9, as t_{ox} decreases, the need for higher κ_{ox} increases. With the continual decrement in size of microelectronics, scientists were forced to look for an alternative that could serve as an interlayer but with a thinner thickness. ZrO_2 is reported to have a κ_{ox} value of 22-25 [94].

The thermodynamic stability of ZrO_2 when in contact with Si is one of the fundamental drivers that made ZrO_2 thin films to be investigated. Different studies were conducted to deduce the stability of ZrO_2 when in contact with Si. Some of the other materials mentioned in the previous section have questionable stabilities. For instance, at high temperatures, SiO_2 is known to form silicate and silicide,

which are undesirable. Usually, the stability of oxide thin films highly depends on the fabrication method.

ZrO_2 thin films deposited on Si using methods such as atomic layer chemical vapor deposition (ALCVD), chemical vapor deposition CVD [95], ALD [96], radio frequency (RF) sputtering [97], metal-organic chemical vapor deposition (MOCVD) [98] and direct current (DC) sputtering [99] found to be stable without forming undesirable compounds, up to temperatures as high as 900 °C.

The band offset between the interlayer and the semiconductor is another indispensable parameter that is directly related to the band gap of the interlayer. The lattice constant of a material is also directly related to its band gap. It is reported that ZrO_2 and Si are practically lattice-matched with lattice constants of 5.07 Å and 5.43 Å, respectively [94]. ZrO_2 has three different crystal structures: monoclinic (m-ZrO_2), tetragonal (t-ZrO_2), and cubic (c-ZrO_2), depending on its operating temperature and whether there is any doping. Yttria, magnesia, and calcium oxide stabilizes t-ZrO_2 and c-ZrO_2 structures [100]. Pure ZrO_2 at atmospheric pressure exhibits a monoclinic structure up to 1170 °C, t-ZrO_2 between 1170 °C and 2370 °C, and c-ZrO_2 between 2370 and 2706 °C. ZrO_2 melts at 2706 °C [101]. Since each crystal structure has a different lattice constant, each has a different band gap value. The band gaps of m-ZrO_2, t-ZrO_2 and c-ZrO_2 are 5.2 eV [102], 6.4 eV and 5.5 eV [103], respectively. This range of band gaps (5 to 6 eV) is ideal for semiconductor applications. The optical properties of ZrO_2 make it compatible with c-Si solar cells as it has a high refractive index (n) of 2.1 [104] and deficient absorption in the visible portion of the spectrum.

From the problems mentioned above regarding the currently used materials and the introduction of the properties of ZrO_2 thin films, it is clear that ZrO_2 has a great potential as an interlayer between n-Si and Al as an electron-selective, passivating layer to reduce the overall ρ_c in c-Si solar cells.

1.8 Aim of This Work

In light of the previous discussions, experiments are conducted to investigate the performance of ZrO_2 when used as an interlayer in c-Si solar cells. To deposit a ZrO_x thin film, the effect of different deposition techniques is investigated. Afterward, elemental characterization is conducted, and interfacial properties of ZrO_x and its performance when used as a contact n-Si / ZrO_x / Al contact are investigated.

CHAPTER 2

THEORY

Adding a thin layer between the metal contact and the base semiconductor, referred to as interlayer, decreases the contact resistivity and improves the charge carrier extraction. This approach is already used in organic semiconductor devices [105] but is yet to be extensively used in the c-Si semiconductor industry [81]. Most currently used interlayers in semiconductors are made of the salts of groups 1A and 2A metals. Fewer studies were made on the use of oxide-based materials for such applications. The study of the interlayer/metal (IM) interface and the interlayer/semiconductor (IS) interface is crucial in improving the device's overall quality.

A question arises: what do interlayers exactly do when they are placed (sandwiched) between a metal and a semiconductor?

Different hypotheses have been proposed to explain how adding interlayers improves the charge carrier extraction and decreases the contact resistance. Ganzorig et al. [106] argued that interlayers dope the semiconductors with which they are in contact and lower the work function of the metal contact. Lowering the work function was also noted by Brabec et al. [107]. Note that the doping process described in this theory is equivalent to heavily doping the rear end of the semiconductor before adding the metal contact. This is further explained in Section 4.1. Other scientists argue that metals occupy the dangling bonds on the surface of semiconductors, referred to as metal-induced-gap-states (MIGS). By separating MS, interlayers render the surface dangling bonds of the semiconductor unoccupied, which is helpful in some MS structures [108]. This is discussed further in the rest of this chapter.

2.1 Contacts and Contact Resistivity (ρ_c)

Metallic contacts are typically used to extract I_L from a solar cell. This necessitates that metals get into direct contact with semiconductors. A discussion regarding metal and semiconductor interfaces must be preceded by an explanation of the band diagram.

2.1.1 Band-diagrams

The energy levels that exist in a single isolated Si atom are discrete. Si atoms have four different energy levels (orbitals) occupied by their valence electrons, namely, s, p_x, p_y, and p_z orbitals. When two identical atoms (e.g., Si) come close to one another, their valence energy levels "interact"; the energy levels hybridize and split into twice the amount of energy levels that existed before. This corresponds to the sp^3 hybrid molecular orbital seen in Si-Si bonds. When two atoms come close to each other, two states arise, which are bonding and anti-bonding. The electrons will be in either one of the states, depending on which requires a lower amount of energy. In the case of Si, the bonding between the atoms has lower energy than the anti-bonding; thus, Si atoms bond together.

Consider a system, for instance, of Avogadro's number (N_A) of Si atoms, at equilibrium inter-atomic distance, from one another (i.e., the nearest atom). This network of atoms will have N_A multiplied by four discrete energy levels as each atom "contributes" with four valence electrons. These hybridized and split newly formed energy levels appear as a continuum of energy levels creating the "band-diagrams" as schematically illustrated in Figure 10. Since the equilibrium inter-atomic distance of Si atoms is 2.35 angstroms (Å), the energy diagram at this distance is considered.

The anti-bonding represents the conduction band (CB), while the bonding represents the valence band (VB). The maximum amount of energy an electron in the VB can have is E_V, while the minimum amount of energy an electron in the CB

can have is E_C. The difference between E_C and E_V is the band gap (E_g). E_g separates the bonding and anti-bonding states apart. No charge carrier is allowed to have an energy value between E_C and E_V, i.e., falls within the E_g.

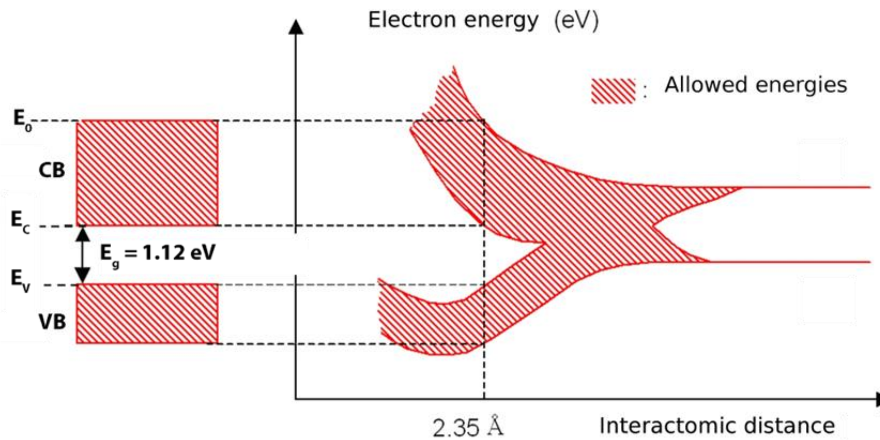

Figure 10. Schematic illustration of the formation of energy bands when many Si atoms bond [109].

Figure 11 shows a schematic representation of the band diagram of intrinsic, n-type, and p-type semiconductors. The vacuum level (E_0) represents a hypothetical level, where the electron is free from the atom and is, practically, outside the material (infinite distance away). The electron affinity (χ) and work function (Φ) represent the amount of energy needed for an electron at the Fermi-level (E_F) and E_C, respectively, to reach E_0.

The probability of finding an electron at a specific energy state could be modeled by the Fermi-Dirac statistical model. For instance, in intrinsic semiconductors at room temperature, the probability of finding an electron is low in the CB and high in the VB. Fermi-level (E_F) is defined as the energy level at 0 K, where all the energy levels beneath it are occupied, and all the energy levels above it are unoccupied.

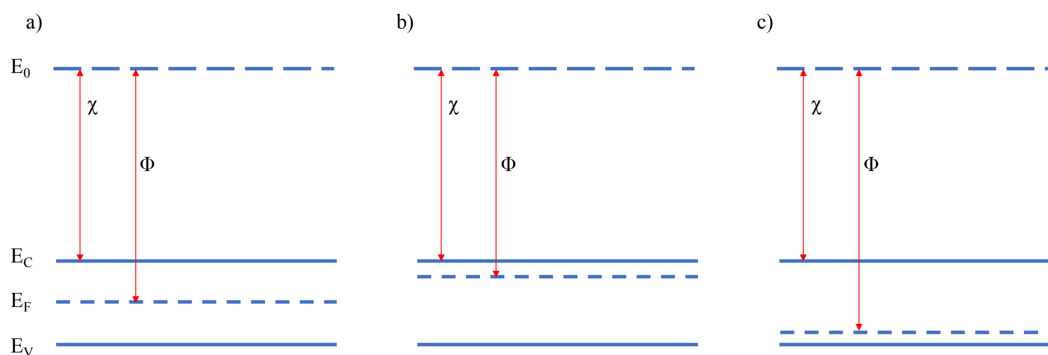

Figure 11. A schematic illustration of the band-diagrams of a) intrinsic, b) n-type and c) p-type semiconductors.

2.1.2 Interfaces

Throughout the rest of the chapter, n-Si in contact with Al will be taken as an example. However, the concepts discussed here are valid for any two solids, with different E_F, in contact with each other.

According to the Schottky-Mott theory [110], when two materials with different chemical potentials, which is another term for E_F, are in contact with each other, their E_F will perfectly align together as a result of the thermodynamic equilibrium (balancing the electric potential that occurs). However, this theory is only valid for ideal interfaces and not applicable to real materials. Schottky-Mott theory, in principle, allows the calculation of the Schottky barrier height (SBH), which is (in this case) the difference between Φ_{Al} and $\chi_{n\text{-}Si}$ [111]. Measured SBH describes the behavior of the contact.

The work function of each material in the structure can be easily calculated. For example, for Si wafers, the Φ can be calculated using 4-Point-Probe (4PP) to measure the R_{SH} first, then multiplying it by the thickness of the wafer (t), which is 200 μm in our case. This gives the electrical resistivity of the wafer (ρ_w). For an n-Si wafer, ρ is the reciprocal of the electrical conductivity (σ), and σ is the product of the charge carrier's mobility (μ), the fundamental electron charge unit (q), and the density of electrons (n_e), as shown in

Eq. 10. μ is known for electrons in Si to be around 1400 $cm^2\ V^{-1}s^{-1}$, and n_e can be calculated from Eq. 11.

$$\sigma = \mu \times q \times n_e$$

Eq. 10

$$n_e = N_c\, e^{\left(-(E_c - E_f)/_{kT}\right)}$$

Eq. 11

, where k is the Boltzmann's constant, T is the temperature, N_C is the effective density of states (known for Si), and E_C is the χ, which is already known in the literature. This leaves E_F to be the only unknown, which is the Φ.

This rule, therefore, as seen in Eq. 10 and Eq. 11, argues that metals with different E_F can change the carrier concentrations at the surface of the semiconductor they are in contact with by bending the semiconductor's bands. Figure 12 shows a schematic of the energy band diagram of Al in contact with n-Si, wherein the values of $\Phi_{n\text{-}Si}$, $\chi_{n\text{-}Si}$, and Φ_{Al} are 4.30, 4.05, and 4.15 eV, respectively. The Schottky-Mott rule suggests that the SBH is the difference between Φ_{Al} and $\chi_{n\text{-}Si}$, which is 0.25 eV. In reality, Vali et al. measured the Al/n-Si Φ_B to be 0.86 eV [112]. This difference is huge from the charge carrier transport perspective.

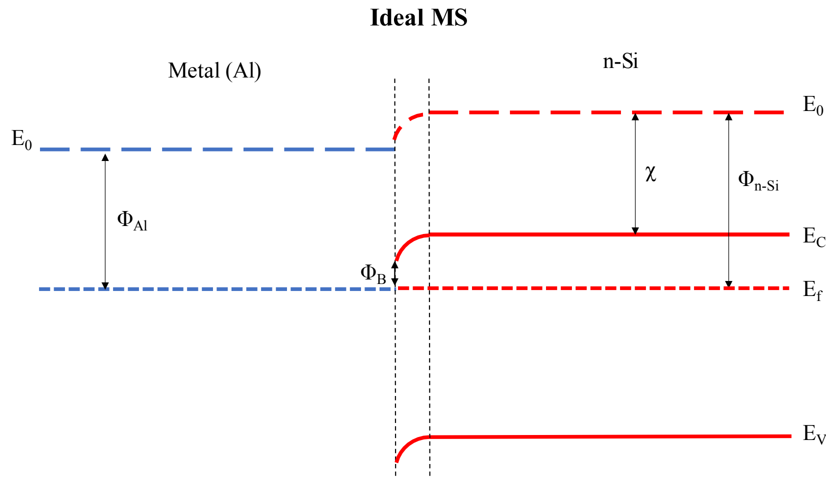

Figure 12. Schematic representation of an energy band-diagram of an ideal MS interface. The two dashed black lines represents the interface.

Less than a decade after Schottky-Mott's publication, it was shown that the Schottky-Mott theory cannot confidently predict the behavior of metals when in contact with a semiconductor due to the so-called surface states, which usually causes Fermi-level pinning (FLP) effect [113]. Surface states are defects at the surface of the crystal. They occur primarily due to dangling bonds at the surface of the crystal and other effects such as the adsorption of foreign particles and impurities [114]. The FLP effect usually causes the measured SBH to differ from the theoretical SBH value obtained by the Schottky-Mott theory.

From an energy band diagram point of view, surface states are called metal-induced gap states (MIGS). Due to the existence of dangling bonds on the surface of a crystal, the crystal no longer becomes ideal, and MIGS appear in the band gap region, which otherwise, is a forbidden region. When a metal gets in contact with the surface of the semiconductor, these unoccupied surface states get occupied by electrons from the metal, which makes them “active”, hence the name MIGS. The MIGS cause the E_F of the semiconductor to pin (FLP), which causes SBH to be unpredictable and accurately known by only measuring it. These MIGS have an effective density which can be signified by a single level called Charge Neutrality Level (CNL), as shown in Figure 13.

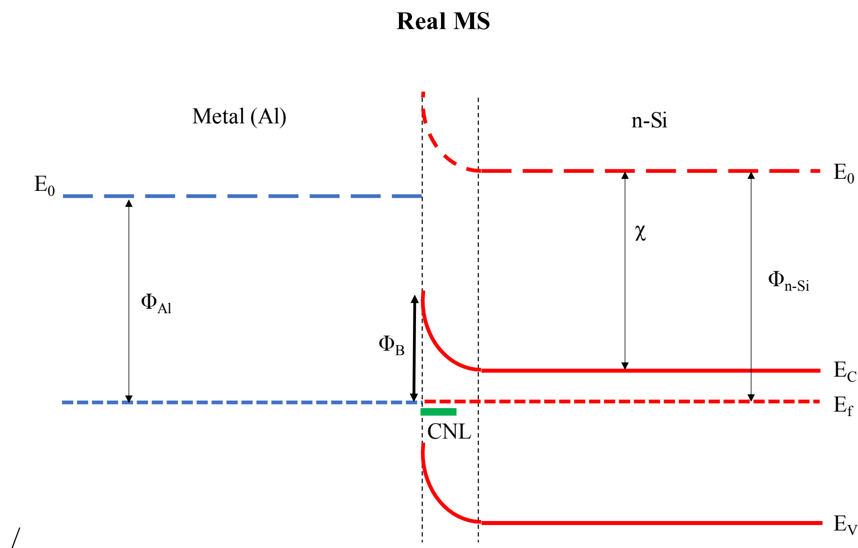

Figure 13. Schematic representation of a real energy band diagram of MS.

When an insulator is placed between MS, it prevents the electrons in the metal from passing to the unoccupied MIGS. So, FLP does not (fully) happen. However, some electrons still pass by the tunneling effect from the metal to the semiconductor. Tunneling will happen regardless of whether there is a passivation layer or not. If there's no passivation, the electrons will "activate" the MIGS (rectifying behavior). If there's passivation, then the electrons tunneling will be extracted by the metal contact (ohmic behavior). This is further explained in the following section.

2.1.3 Ohmic and Rectifying Contacts

SBH does not allow the majority charge carriers to flow through the interface when a metal is in contact with a semiconductor. Counterintuitively, this effect is mostly independent of the metal's E_F and more dependent on the semiconductor's doping concentration. When in contact with most metals (i.e., Al), n-Si tend to have a large SBH of about 0.66 eV [115]. SBH above 0.30-0.40 eV is considered to be high and causes rectifying behaviors in contacts. Below 0.3 eV, for a normally operating semiconductor device with a high dopant concentration (~10^{20}/cm^3), the crystal behaves as ohmic. For a given barrier height, the voltage range in which the current will depend on the contact will vary. Such that after a threshold bias voltage, the current will depend on the substrate, and the whole device will give an ohmic response.

In the voltage range (mostly after 0.3 V) in which the current depends on the contact, the current's dependence on the bias voltage is exponential. If the barrier is small enough, the rectifying behavior may not be visible, and a misleading, ohmic behavior will be observed. The reason is that at small voltages $e^V \approx 1+V$, which approximates the diode equation (Eq. 3) to $I \cong I_0 \left(\frac{q}{kT} V\right)$; I varies (almost) linearly with V; ohmic behavior.

There are many forms of rectifying behaviors in contacts; the Schottky diode behavior is a typical example that was faced throughout this study. A rectifying behavior is when the I-V relationship (when plotted) is not linear; while in an ohmic contact, the I-V relationship is linear. An ohmic behavior means that the current going in the forward direction is the same as the current going in the reverse direction, which is required in contacts of solar cells because it facilitates the extraction of the charge carriers with a much lower probability of recombination occurring before extraction, as opposed to rectifying behavior.

A discussion about ohmic and rectifying behaviors of contacts necessities mentioning the following: as the contact's area increases, the ohmic behavior increases. This could be specious, and indeed, in the era of larger device sizes, Al was used predominantly as a contact without showing any apparent reduction in resistance. This is no longer the case as semiconductor devices are shrinking in size. A typical way of checking the behavior of metallic contacts on top of semiconductors is examining their I-V curves. Figure 14 shows the IV curves for hypothetical ohmic and Schottky contacts.

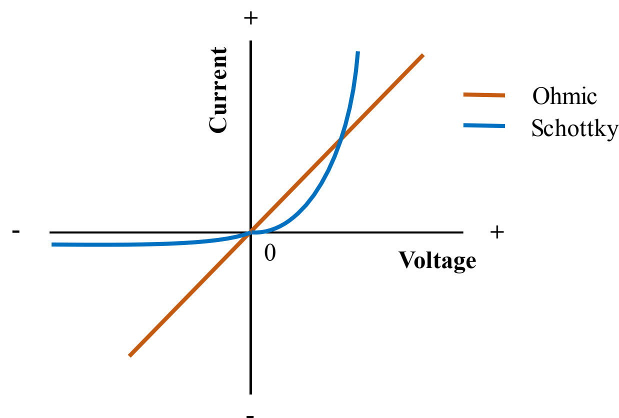

Figure 14. Hypothetical I-V curves for ohmic and Schottky contacts.

2.1.4 Charge Carriers Transport

SBH is denoted as $\Phi_{B,n}$ for n-type semiconductors (n-Si) when in contact with a metal (Al). There are three main conduction mechanisms, for a given $\Phi_{B,n}$ height, for the charge carriers (electrons) to cross that $\Phi_{B,n}$. These conduction mechanisms are thermionic emission (TE), thermionic-field emission (TFE), and field emission (FE). Schottky contacts typically have a large $\Phi_{B,n}$, so the charge carriers use the TE way to cross it. TE means that the charge carriers simply "jump" over the barrier. For ohmic MS contacts, where the $\Phi_{B,n}$ is relatively small, charge carriers use the FE mechanism (tunneling) as they need less energy to cross the $\Phi_{B,n}$. If the $\Phi_{B,n}$ has a relatively average height, charge carriers use a combination of TE and FE that is the TFE wherein they cross the barrier by being excited to a higher energy state and then tunnel through the rest of the barrier. These mechanisms are schematically illustrated in Figure 15. Two of the methods commonly used to calculate ρ_c are the Transmission Line Method (TLM) and Cox-Strack Method CSM (ρ_c). In this work, the CSM method was used.

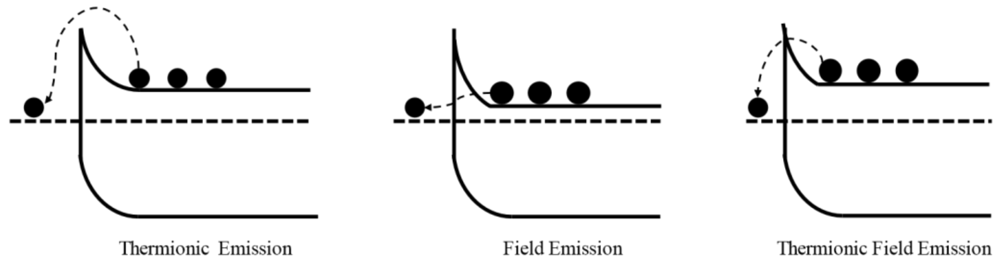

Figure 15. Carriers transport mechanisms in MS junctions.

2.2 Cox and Strack Method (CSM)

The Cox-Strack Method (CSM) is reported to be more accurate when measuring the resistivity of a contact material [116]. Conventionally, a shadow mask that has circular holes with different diameters is used, as shown in Figure 16. To verify that ZrO_x is an electron-selective material, structures of Al/ZrO_x/p-Si/Al with different thicknesses of ZrO_x were prepared and measured. The results showed

Schottky behavior of the top contact, which led to the conclusion that ZrO_x is not a hole-selective material. Other measurements were taken for Al/ZrO_x/n-Si/ZrO_x/Al structures, and the results showed an ohmic behavior of both contacts (top and bottom). This verified that ZrO_x is an electron-selective material and will work best on n-Si solar cells. Note that Al exhibits Schottky behavior when used as a contact on n-Si. The following points summarize the measurement procedure:

1. To fabricate the structure, double-side-polished (DSP), low-resistivity (1-3 Ω.cm), phosphorus-doped crystalline Si wafer (n-Si) was used where ZrO_x followed by Al were both deposited on both sides of the wafer, creating a symmetrical structure (Figure 32).
2. For each contact (top and rear), measurements of the current at various applied voltages were taken.
3. The slope of the straight-line created from step 2, i.e., the resistance, for each contact was taken.
4. Total resistance (R_T) – resistance of the substrate (R_S) vs. 1/area of the contacts was plotted.
5. Finally, the slope of the line created from step 4 corresponds to the ρ_c.

The I-V curves show the total resistance of the entire system (R_T). R_T comprises the substrate's resistance (R_S), the contacts' resistance (R_C), and the resistance of the wires and the device itself (R_0). When measuring different contacts, the equipment used and the surrounding conditions were the same; hence, R_0 is assumed to be constant.

$$R_T = R_S + R_c + R_0$$

Eq. 12

In the CSM, the current is assumed to propagate throughout the substrate in increasingly wider circles, i.e., spreading resistance, depending on the diameter of the contact. To know R_S, the resistivity of the substrate, ρ_s is measured before creating the structure. Using a 4-point-probe (4PP), the sheet resistance can be

measured which, when multiplied by the thickness of the substrate, gives the ρ_s. Cox and Strack described the spreading resistance in the substrate (R_S) as:

$$R_S = \frac{\rho_s}{2d} * B$$

Eq. 13

and

$$B \sim \frac{2}{\pi} * tan^{-1}\left(\frac{4t}{d}\right)$$

Eq. 14

, where *t* is the thickness of the substrate and *d* is the diameter of the contact. It is worth noting that *B* has an exact expression, which does not always give a more precise estimation of R_S rather the accuracy of the expression depends on a geometrical factor of the contact [117]. R_C is a function of the diameter of the contact as

$$R_c = \frac{\rho_c}{\pi r^2}$$

Eq. 15

Rearranging Eq. 12 to be R_T - R_S = R_C + R_0, where it could be treated as an equation of a straight-line so that (R_T-R_S) is y, R_0 is a constant, ρ_c is m, and $1/\pi r^2$ is x. Hence, plotting the R_T-R_S vs. 1/area of the contacts yields ρ_c as the slope of the graph. This method was followed to calculate the ρ_c in this study, which is laid out in Section 3.5.

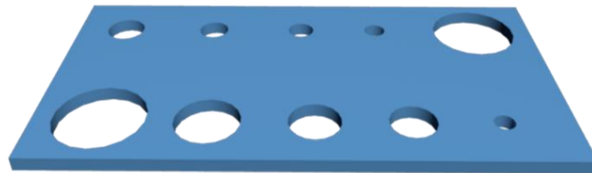

Figure 16. Schematic representation of the shadow mask used in CSM

CHAPTER 3

DEPOSITION AND CHARACTERIZATION OF ZIRCONIA THIN FILMS

3.1 Solution Processing

Wet chemical deposition (solution processing) was the leading candidate technique for the deposition of ZrO_2 on Si as it is a more facile, rapid, and cheaper method than vacuum-based techniques. The spin coating technique is reported to reach a thickness of 180 nm [118] and as low as 17 nm [119]. Henkel uses Bonderite M-NT-1 (BM1) for coating steel products with a thin layer of ZrO_2 to protect steel from oxidizing. The exact composition of BM1 is not disclosed; however, the main ingredient is hexafluoro zirconic acid (HFZ) as mentioned in the technical data sheet [120]; hence HFZ was also investigated on its own. The chemical reaction expected to occur when HFZ is coated on Si is as follows:

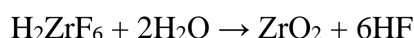

$$H_2ZrF_6 + 2H_2O \rightarrow ZrO_2 + 6HF$$

Eq. 16

Numerous experiments were conducted to deposit ZrO_2 using BM1 and HFZ by spin, spray and dip coating techniques. The main challenge was to control the thickness obtained by these methods. For miniaturization purposes, the thickness of the needed ZrO_2 thin film is 1-5 nm. Such low thicknesses are hard to achieve without a vacuum system. Another challenge was obtaining a continuous ZrO_2 thin film rather than coarse discontinuous micro-particles. Another issue was the poor adhesion of the deposited ZrO_2 on Si.

The HFZ used was 50% concentrated in water. Spin coating HFZ on a c-Si subjected to Radio Corporation of America (RCA) cleaning process followed by

HF-etching. This resulted in a visible coating, as shown in Figure 17, and Raman analysis was conducted for chemical analysis, as shown in Figure 18.

From literature [121] the Raman peaks for ZrO_2 are located at 222, 306, 333, 347, 380, 475, 502, 536, 558, 615, 637 and 756 cm^{-1}. The peaks found in this sample were at 227, 303, 430, 528, 621, 671, and 810 cm^{-1}. The 528 cm^{-1} peak corresponds to the c-Si. Figure 18 shows the results, which confirmed the existence of ZrO_2.

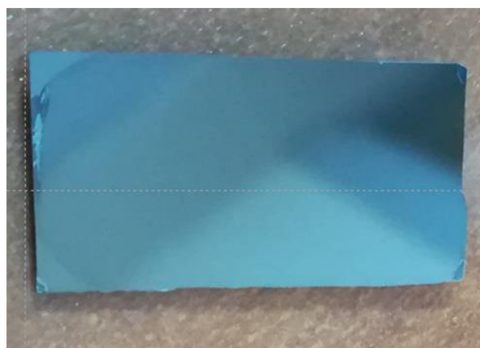

Figure 17. Visible coating (at the top left edge) on a c-Si wafer by HFZ solution using spin-coating technique.

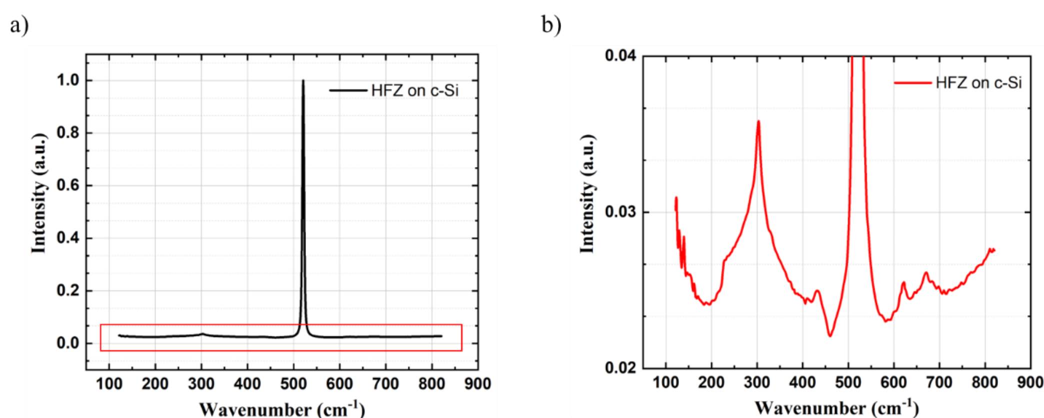

Figure 18. Normalized Raman analysis for the HFZ spin-coated c-Si sample a) the full spectrum and b) focused on the peaks related to ZrO_2.

From thermogravimetric analysis (TGA) in Figure 19, the following points are deduced:

- A loss of 56% of the original mass is expected if there is Zr.
- A loss of 40% of the original mass is expected if there is ZrO_2.

- A loss of 19% of the original mass is expected if there is ZrF_4.
  (Note: ZrF_4 has a melting point of 910 °C)
- A mass loss of 30% is observed as 4.24 mg (out of 6.04 mg) were left.

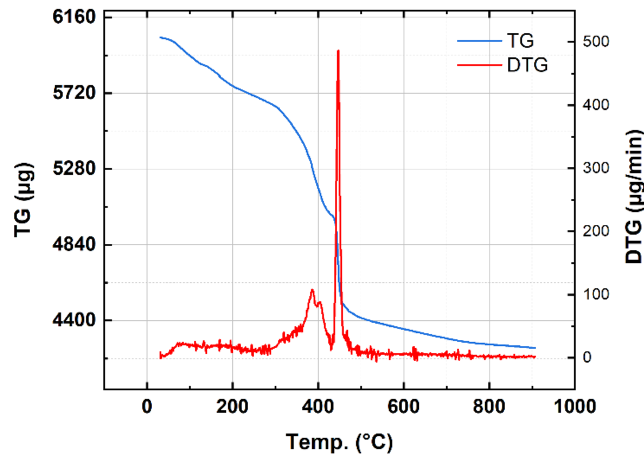

Figure 19. TG and DTA analysis of HFZ in powder form. At 425 °C, physically attached water in HFZ is evaporated.

As for BM1 deposition, Figure 20 (a), (b), and (c) show SEM images of samples S-43, S-45, and S-46, wherein BM1 is spray, spin, and dip coated, respectively. As seen from the provided SEM images, a continuous thin film is never achieved; instead, discrete and spread-out particles are found to be deposited. The aforementioned chemical solutions and deposition techniques did not successfully deposit ultra-thin layers of ZrO_x.

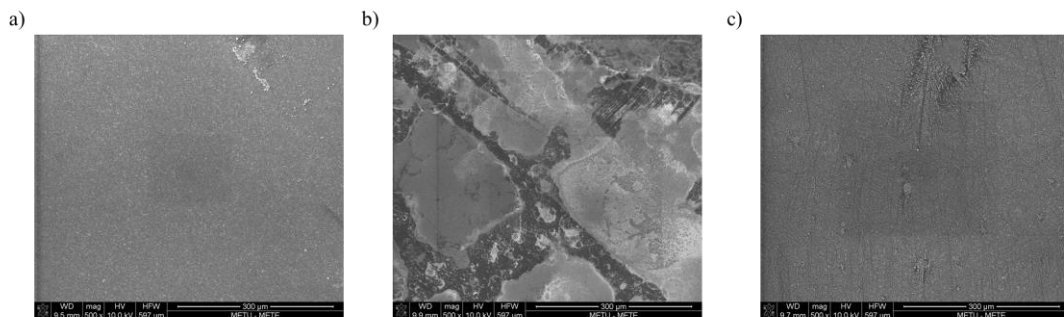

Figure 20. SEM images of BM1 a) spin-coated, b) spray-coated, and c) dip coated on c-Si. The coating parameters and temperatures are presented in Table 2.

Table 2. Summary of the solution processing attempts for ZrO_x deposition.

Sample	*Solution*	*Method*	*Cycles*	*Annealing*	*Comments*
S-43	BM1	Spin	5	130 °C	5 min anneal
S-45	BM1	Spray	5	130 °C	Hot-plate
S-46	BM1	Dip	1	150 °C	Hot-plate

Zirconium acetate hydroxide (ZRAH) pellets functioned as a solute in acetic acid to prepare another precursor to deposit ZrO_2 thin films on Si. Solvents (ethanol, isopropanol, methanol, and acetone) other than acetic acid are investigated, and acetic acid is found to be the most efficient. Figure 21 shows SEM images of 11 wt.% Zr concentrated ZRAH solution (10% diluted acetic acid as solvent) coated on c-Si. The coating is practiced by a spin coater at a speed of 3000 rpm for 30 seconds. The sample is dried at 90 °C for 20 minutes, then annealed in air to turn Zr into ZrO_x (oxidation) at 200 °C for 15 minutes. Experiments are conducted with different temperatures, timings, spinning parameters, and concentrations. The sample shown in Figure 21 gave the SEM images of the most homogeneous and continuous coatings, despite discontinuities. From that SEM image (Figure 21), it is believed that a continuous thin film was formed but soon broke due to the sudden temperature changes [122]. This led to further experiments, where the only changing parameter is the rate of change of the coating/substrate's temperature. The SEM images showed that the structures obtained are identical when gradually and rapidly heated or cooled. Another explanation is the poor wetting of the ZRAH on Si.

Throughout all the solution-based deposition experiments, the coating is easily removed when touched (poor adhesion). Also, it was not practical to measure the thickness of the coating after each deposition cycle. However, since it was visible to the naked eye, it was certain that the coating was more than the required thickness (a few nm).

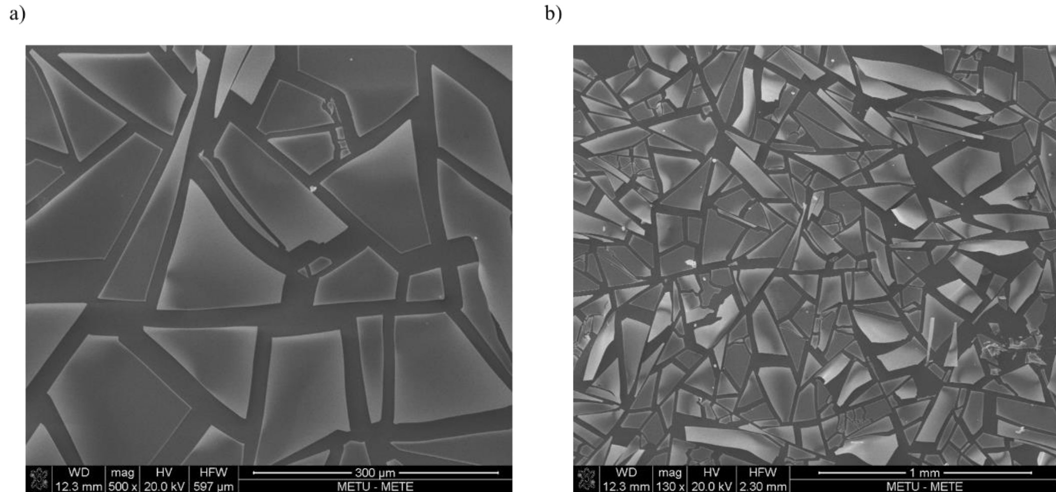

Figure 21. SEM images of ZRAH coated on c-Si using spin coating technique at a) 300 µm, b) 1 mm scales for the same sample.

Wet chemical deposition of ZrO_2 onto Si is found to be a challenging endeavor as there are many parameters to be considered. It is also worth mentioning that only a few studies regarding the solution deposition of ZrO_2 thin films on Si exist in the literature [123].

3.2 Atomic layer deposition (ALD)

One of the most precise ways to deposit a thin film is atomic layer deposition (ALD). This technique allows the deposition of a film as thin as one atomic layer. Sequential gas phase precursors are pumped into the reaction chamber, as in other chemical vapor deposition (CVD) techniques. In fact, ALD is considered a subclass of CVD [124]. ALD of ZrO_2 on c-Si was carried out in NÜRDAM, Turkey.

Tetrakis (dimethylamido) zirconium (IV) (TDMZr) with 99.99% purity from Sigma-Aldrich was used as the main precursor, and H_2O as the oxidizing agent. In this self-limiting reaction, the TDMZr is allowed to pass in the pre-vacuumed reaction chamber, where the substrate is, to react with the surface for a time called the dose-time. This is followed by a "purge time" where N_2 gas (or

another inert gas) is passed to evacuate the excess TDMZr in the reaction chamber after all the reaction sites on the substrate react with the Zr-precursor. Afterward, H_2O gas (or O_2 gas) is pumped into the reaction chamber during another dose-time, not necessarily the same, where the free Zr bond accepts the O molecules and forms ZrO_2. This dose-purge-dose-purge is called an ALD cycle. The required exact thickness can be achieved by controlling the number of cycles. Figure 22 shows a schematic representation of the ALD process. Xin Wang et al. discussed the ALD process for the TDMZr precursor [125]. Table 3 summarizes the experimental design utilized in this thesis to deposit ZrO_2 on c-Si using TDMZr precursor.

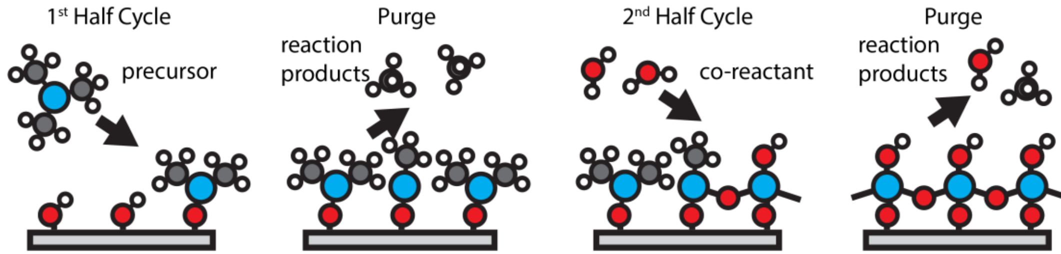

Figure 22. Schematic representation of an ALD cycle [126].

Table 3. Design of experiment for the ALD of ZrO_2 on c-Si using TDMZr.

	TDMZr			*H_2O*			*Device Temp*			*Device Parameters*	
Experiment	*Temp (°C)*	*Time (msec)*	*purge (s)*	*Temp (°C)*	*Time (msec)*	*purge (s)*	*Tsub (°C)*	*Twall (°C)*	*Tlines (°C)*	*N_2 (sccm)*	*Cycles*
E-1	95	15	15	RT	15	15	200	110	100	20	150
E-2	95	100	20	RT	20	20	200	110	100	20	150
E-3	95	100	20	RT	20	20	200	200	100	50	300
T-1	110	500	40	RT	50	40	200	200	150	50	150
T-2	110	500	40	RT	50	40	150	150	150	50	150
T-3	110	500	40	RT	50	40	175	175	150	50	150

XPS analysis is conducted for all the samples. Only sample T-3 showed the existence of ZrO_x. The XPS signal obtained from sample T-3 is shown in Figure 23. Peaks at 184 eV and 182.1 eV (Figure 23 (a)) corresponds to Zr $3d_{3/2}$ and Zr $3d_{5/2}$ respectively. Figure 23 (b) shows the peaks for the O 1s at 529.7 eV and another hump at 531.1 eV. The former peak corresponds to the O – Zr bond, while the latter to the O-H bond [127]. However, the peaks of Zr 3d shown in Figure 23

(a) are flatter and have more noise than in the literature. This could be due to the excess presence of carbon on the surface, the low number of scans when the XPS measurements were taken, or an indication of the presence of Zr suboxides and other Zr compounds [128]. Alas, ALD experiments stopped due to COVID-19 restrictions.

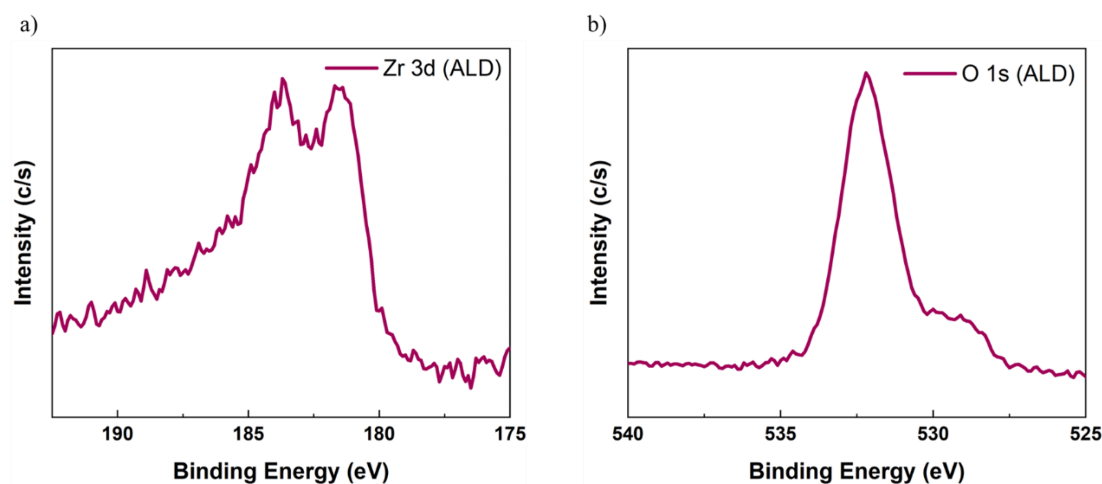

Figure 23. The XPS signal for a) Zr 3d and b) O 1 obtained from characterizing ZrO_2 thin-layer that is deposited on c-Si using ALD.

3.3 Thermal Evaporation

3.3.1 Experimental procedure

Physical vapor deposition (PVD) is a common method for thin-film deposition that many techniques can practice. One of these techniques is thermally evaporating a metal (or any target material that this technique could evaporate) in a vacuum chamber and placing the substrate on top of the molten metal allowing it to deposit on the substrate's surface when the molten metal starts to evaporate. In PVD, a thickness monitor crystal is usually placed next to the substrate to measure the thickness of the deposited layer. Calibration is needed during the first few trials to determine the "tooling factor" of the crystal in the system. This tooling factor accounts for the displacement between the crystal and the substrate.

To evaporate the metal (or any target material), the metal pellet is placed in a holder of a high melting alloy, usually, a tungsten (W) based alloy, and then a high electric current is allowed to pass through it. These holders are made of different shapes (e.g., wires, boats, crucibles), alloys, and sizes depending on the target material to be evaporated.

Since ZrO_2 has a melting point of 2,715 °C under atmospheric pressure, thermal evaporation is not recommended [129]. Instead, we used zirconium metal (Zr) pellets, which have a melting temperature of ~ 1,702 °C at a vacuum pressure of 10^{-6} torr [130], in a 0.030″ (0.762 mm) thick W basket. To deposit 1 Zr pellet (0.090 g), the vacuum level is brought to about $2x10^{-6}$ torr then a current of 100 A (420 watts) is slowly allowed to pass through the wire that contains the Zr pellet. The Zr metal heats up, melts, wets the basket, and evaporates at a typical rate of 0.25 – 0.30 Å/s. A schematic view of the thermal evaporation setup is provided in Figure 24 (a), and an image of a sample after the deposition of a thick layer of Zr metal by thermal evaporation is provided in Figure 24 (b). The substrate edges are covered using Kapton tape, thus showing the difference between the Zr-coated and the bare substrate.

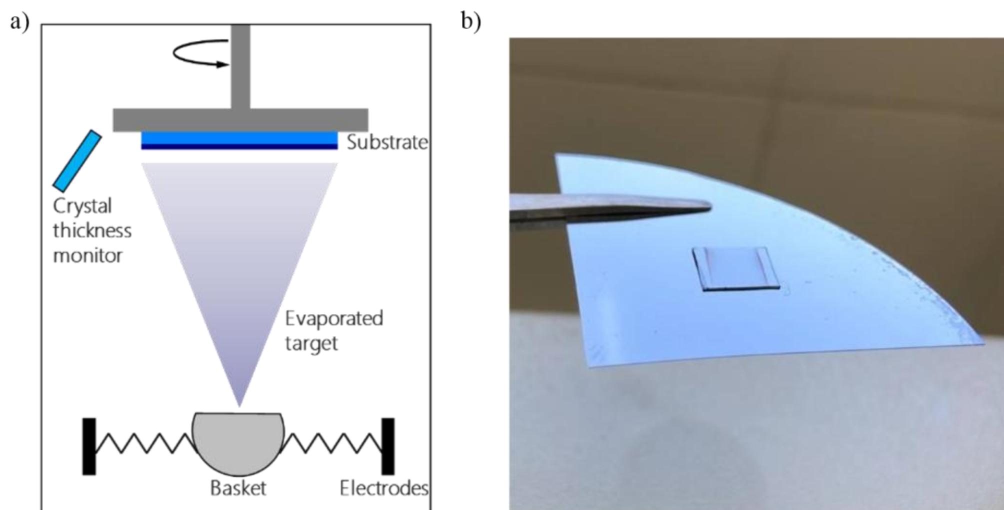

Figure 24. a) Schematic view of the thermal evaporation setup and b) a virtually thick layer of Zr metal deposited on a c-Si substrate by thermal evaporation.

3.3.2 Results and discussion

XPS analyses are conducted for two samples. One is annealed in air at 300 °C for 20 minutes (E8), and the other is not subjected to any heat treatment after deposition (E9). The XPS depth profiles of samples E8 and E9 are shown Figure 25 (a) and (b), respectively. A remarkable decrease in the carbon content and an increase in the oxygen content are observed for the annealed sample (E9) compared to the as-deposit sample (E8).

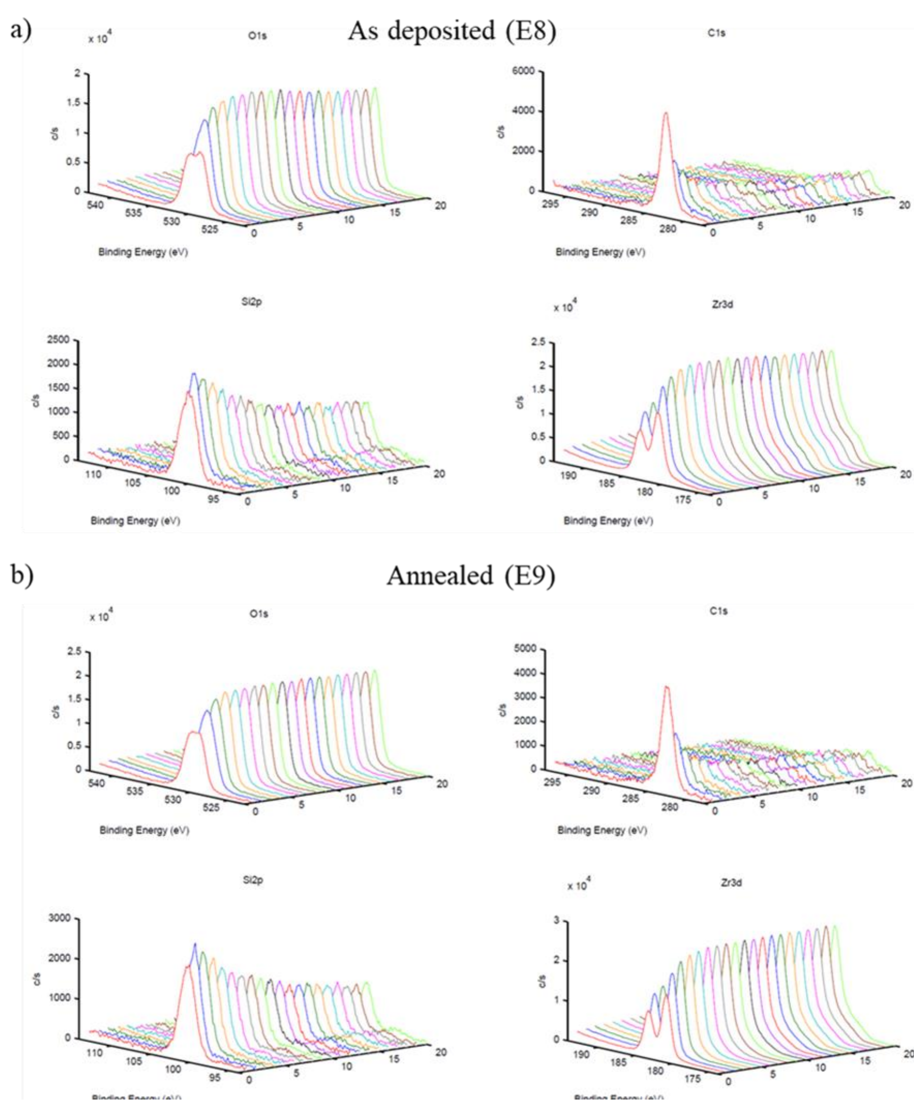

Figure 25. The XPS depth profiling for thermally evaporated Zr on c-Si a) as-deposited (E8) and b) annealed at 300 °C for 20 min (E9).

Experiments are conducted to determine a suitable annealing temperature. Table 4 summarizes some of these experiments and their results where 6 nm of ZrO_x is deposited onto n-Si. Considering the lifetime values Wan et al. [93] reported, there is clear room for improvement. However, Wan et al. used ALD and deposited 18-20 nm thick, perfectly stoichiometric ZrO_2, while the deposition thickness intended in this work is 3 nm of nonstoichiometric ZrO_x. Few to no other data in literature used ZrO_2 on c-Si solar cells, as mentioned in Chapter 4.

Table 4. Different parameters for different samples for ZrO_x films and their relative lifetime and iV_{OC} measurements.

	Annealed for 20 min				*Annealed at 400°C*			
	As deposited	***300°C***	***400°C***	***600°C***	***10 min***	***20 min***	***40 min***	***60 min***
iV_{OC} (mV)	536.3	546.2	574.1	535.3	577.0	561.2	551.0	552.3
Lifetime (µs)	4.42	12.46	40.81	5.95	56.88	29.65	16.37	17.77

3.4 Electron Beam (E-beam)

3.4.1 Background

The primary purpose of switching from thermal evaporation to an e-beam evaporation system (e-beam) is to melt down and evaporate pure and stoichiometric ZrO_2, unlike thermal evaporation, where Zr is evaporated and then annealed to react with air and oxidize to sub-stoichiometric ZrO_x. Figure 26 (a) shows a schematic view of the e-beam vacuum chamber while Figure 26 (b) shows a vivid image of 50 nm ZrO_x coated on c-Si using e-beam.

In an e-beam system, first, the vacuum pump creates vacuum (~ 10^{-5} torr) inside the chamber, then the current is passed through the target filament, creating an electron

beam stream, where magnetic fields control its direction. The electron stream bombardment of ZrO_2 pellets melts them (locally) and then evaporates them, creating zirconia vapor that condenses and deposits on the substrate. The substrate is rotated during deposition to achieve a homogeneous film. This deposition technique allows the deposition of films as thin as a few angstroms (Å). E-beam evaporation is used for the deposition of ZrO_x while fabricating a solar cell which is discussed in Chapter 4.

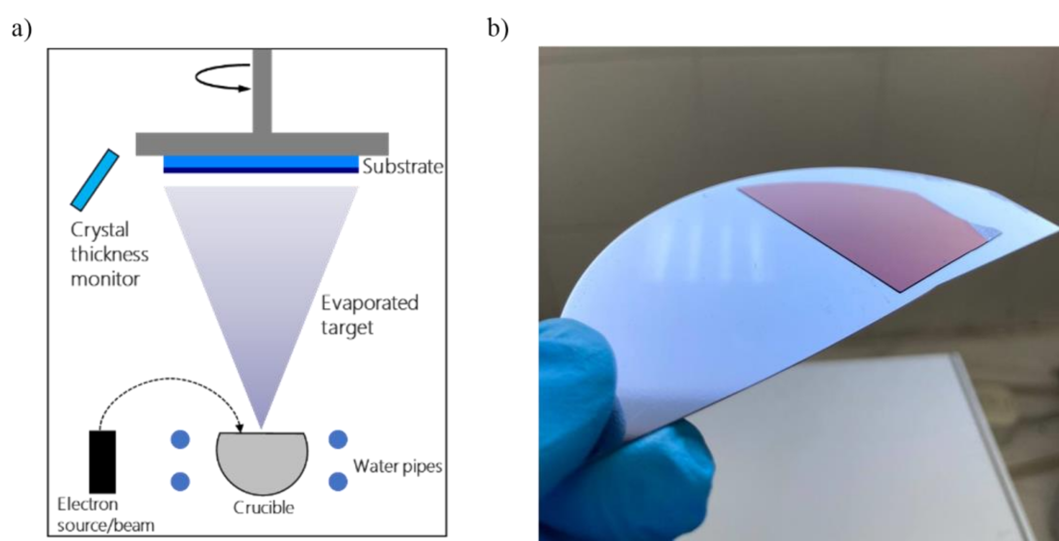

Figure 26. a) Schematic of the e-beam setup. b) 50 nm thick ZrO_x film (purple) coated using e-beam onto a c-Si substrate.

3.4.2 Results and discussion

The device is first calibrated using its crystal monitor to deposit a 50 nm thick ZrO_x on an HF-treated c-Si wafer. The shadow mask (Figure 16) is placed on a part of the wafer to create a step. The difference in height between the bare c-Si and the 50 nm ZrO_x coated Si is determined using the Dektak device, and the tooling factor is set accordingly. In order to confirm the thickness, more trials are made for different thicknesses, and an ellipsometer is used for further confirmation.

The spectrometric ellipsometer (SE) analysis for one of these trials for a 3 nm thick ZrO_x layer is shown in Figure 27. The fitting accuracy is reported to be 0.999 with

a refractive index (n) of ~ 2 and a band gap (E_g) of ~ 5.2 eV. These results are in alignment with the results in the literature [131].

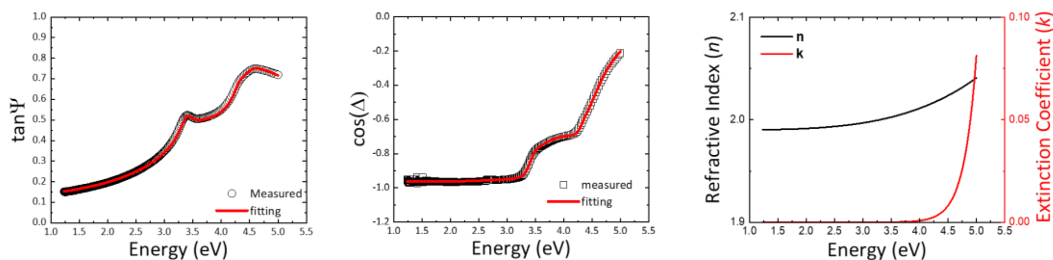

Figure 27. The SE fittings of a) tan (Ψ), b) cos (Δ) vs Energy and c) the final results where n and k are calculated.

XPS analysis is conducted for 1 nm and 50 nm thick ZrO_x coated on Si, showing information regarding the elements bonding and stoichiometry for the 1 nm thick layer and the survey scan and depth profile for the 50 nm thick layer.

For the 1 nm thick ZrO_x, high-resolution XPS analysis showed that the Zr $3d_{5/2}$, Zr $3d_{3/2}$, and O 1s peaks are located at 181.9, 184.2, and 529.7 eV, respectively. The O 1s XPS peak can be deconvoluted into two peaks; one corresponds to the Zr – O bond and the other to the C – O bond at 529.7 and 531.3 eV, respectively. These results agree with the results found in the literature [132]. Figure 28 (a) and (b) show the XPS of the core level spectra for the Zr 3d and O 1s peaks, respectively. It is believed that the Zr $3d_{5/2}$ orbital is the orbital responsible for the bonding with O. The fitting was done using CasaXPS software. Shirley's background was used. For the Zr 3d orbitals, the distance between the peaks of orbital $3d_{5/2}$ and $3d_{3/2}$ was fixed to be 2.4 eV. A typical mixture of the product of Gaussian and Lorentzian functions is used in the fitting; 70% Gaussian and 30% Lorentzian, GL (30).

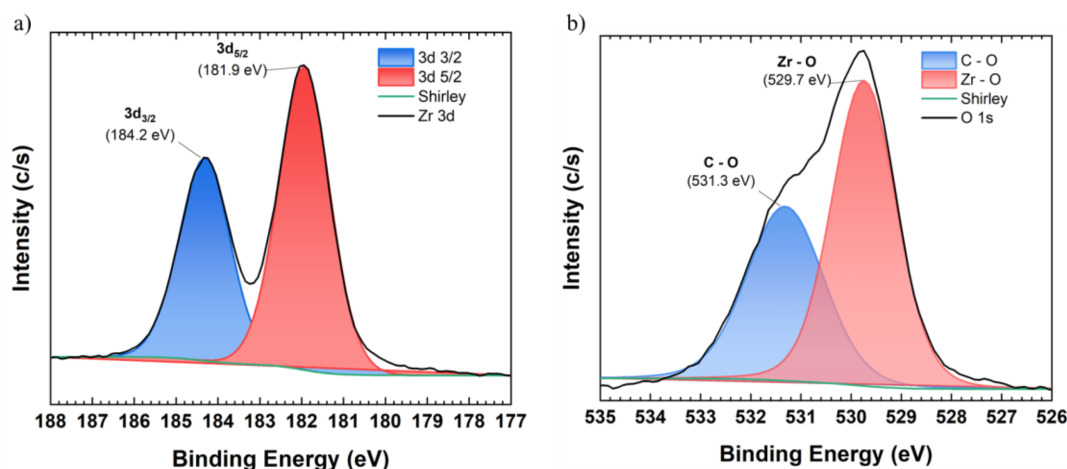

Figure 28. The XPS core level spectra of 1 nm thick ZrOx on n-Si for a) Zr 3d and b) O 1s.

The survey scan for the 1 nm thick ZrO_x layer in Figure 29 (a) shows the existence of oxygen (O), carbon (C), and Zr and the absence of any other element. The depth profile for the 50 nm ZrO_x on Si shows a drastic decrease in C after the first 3 min sputtering and an increase in the Zr content, as shown in Figure 29 (b). Results are taken every 3 min for five intervals.

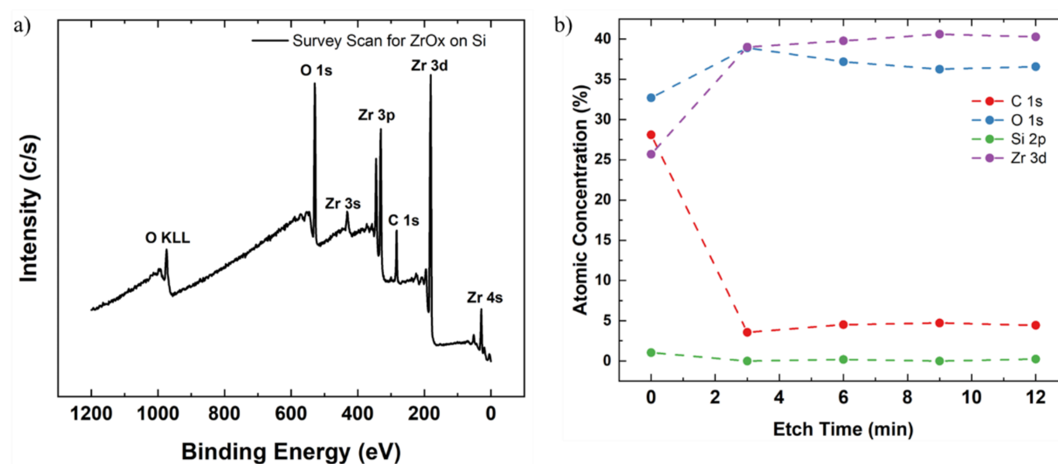

Figure 29. a) XPS survey scan for 1 nm thick ZrOx deposited on n-Si by e-beam and b) XPS depth profile of the 50 nm thick ZrOx coated on n-Si.

To determine the crystallinity of the deposited film, the X-ray diffraction (XRD) method is used on a 50 nm ZrO_x coated glass. Glass is chosen due to its amorphous structure, which will prevent interference of any diffraction peaks with ZrO_x peaks.

Figure 30 shows that the layer is strictly amorphous and exhibits no crystallinity. This is expected as the layer is relatively thin for the atoms to align, especially in the absence of any heat treatment. Grazing-XRD for a 5 nm thick ZrO_x layer yielded no results as the layer was thinner than the limit of the device.

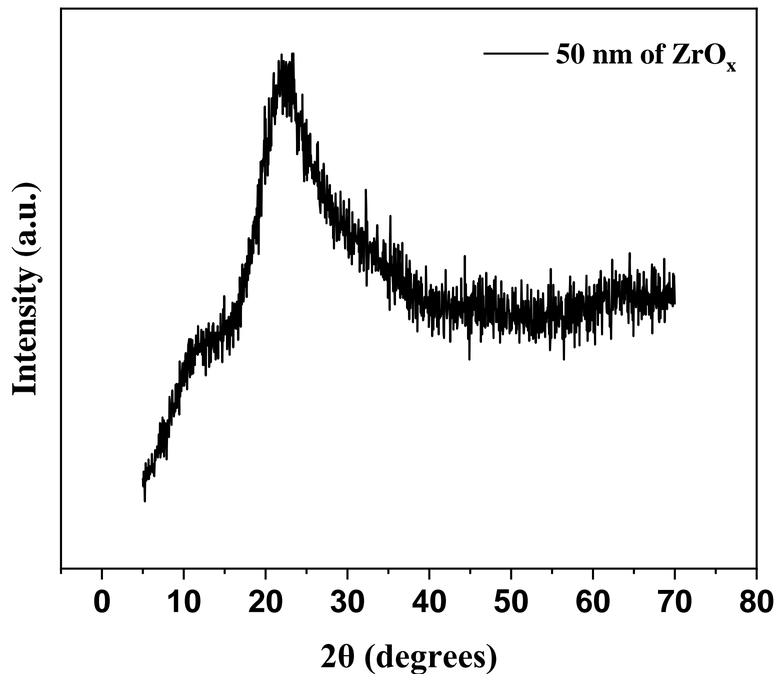

Figure 30. XRD result for 50 nm thick ZrO_x film coated onto glass substrate.

The optical properties of 50 nm thick e-beam deposited ZrO_x films are investigated. Their optical band gap, spectral reflectance, and absorbance are calculated and presented in Figure 31 (a) - (c). The optical band gap is estimated to be 6.13 eV. Wong et al. reported band gaps between 6.20 to 6.50 eV according to different oxidation times for ZrO_x [102]. The band gap is expected to increase with increasing the film's thickness as the film behaves more like the bulk material. This could explain the difference in band gaps found by the ellipsometer analysis of the 3 nm thick ZrO_x film and the 50 nm thick ZrO_x film. It could also be attributed to the different crystal structures of ZrO_2, as discussed in Section 0. The transmittance was above 80%, starting at 230 nm and reaching more than 93% at a wavelength of 800 nm. On the other hand, the absorbance shows the opposite behavior of the transmittance as expected.

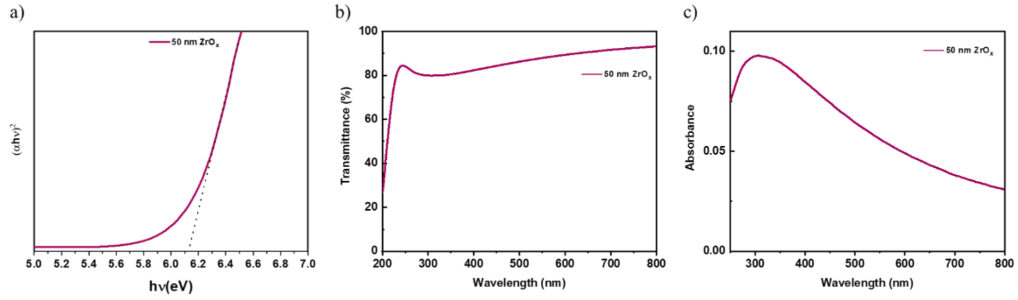

Figure 31. a) Tauc plot, b) transmittance, and c) absorbance of 50 nm thick ZrO_x film.

3.5 Contact Resistivity Measurements

The c-Si wafer is first subjected to the RCA cleaning process, a standard process to clean native oxides, metallic, and organic impurities off the surface of Si wafers [133]. The wafer is then subjected to 5% diluted HF to remove the native SiO_2 layer before loading the wafer into the e-beam chamber. To find the optimal thickness of ZrO_x that will give the lowest contact resistance to a DSP, a lightly doped n-Si wafer with R_{sq} of 2.9 Ω/sq and a thickness (t) of 200 μm was used. It is important to note that the wafer used in manufacturing the solar cell (mentioned in Chapter 4) is textured, not polished.

As illustrated in Figure 16, the shadow mask contains different circles with different diameters, from 0.8 mm to 3.5 mm. This mask is attached to the top of the HF-etched Si wafer and kept in position by Kapton tape.

After reaching a vacuum level in the order of 10^{-5} torr, ZrO_2 pellets are evaporated using the e-beam evaporation system. Without breaking the vacuum, 200 nm of Al is thermally evaporated on the ZrO_x. The thickness is controlled by the calibrated crystal thickness monitor inside the chamber. The system is then allowed to cool and vented back to normal pressure using N_2 gas. The structure is then flipped on the other side, and the same process is applied without using the shadow mask on the backside as full area coverage was intended. The layer deposited on the top and bottom, while different in areas, are equal in thicknesses for a given sample.

However, for different samples, different thicknesses of the ZrO_x layer are deposited, while the thickness of the Al is kept the same at 200 nm. The 3D schematic of the final CSM structure is shown in Figure 32. The measurements are taken from the top of each contact and the back of the whole structure.

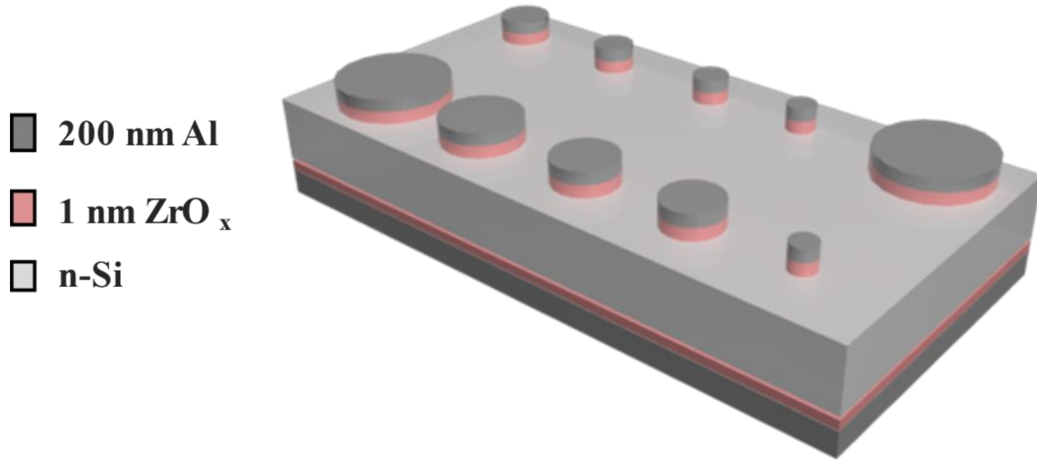

Figure 32. 3D schematics of the CSM structure are used to measure the I-V curves.

An example of the ρ_c measurement for one sample that produced the lowest ρ_c is provided in this section. The structure of that sample is shown in Figure 32. The thickness of the substrate (*t*) was 0.02 cm, and from the 4PP, R_{SH} was found to be 146 Ω/sq. R_S was found for each contact using equations Eq. 13 and Eq. 14, as discussed in Section 2.2. Eq. 17 gives the formula for calculating ρ_s from the R_{SH} and *t* of the wafer. Table 5 shows each contact in the shadow mask with its corresponding diameter and the calculated B values and R_S for each contact. ρ_s is constant (2.90 Ω) as the same wafer was used for all contacts.

$$\rho_s = R_{SH} * t$$

Eq. 17

Table 5. The shadow mask's contacts diameters, B values and R_S.

Contact #	*diameter (cm)*	*B*	ρ_s (Ω)	R_S (Ω/cm)
1	0.35	0.14	2.90	0.59
2	0.25	0.20	2.90	1.14
3	0.2	0.24	2.90	1.76
4	0.18	0.27	2.90	2.14
6	0.35	0.14	2.90	0.59
9	0.125	0.36	2.90	4.20
10	0.16	0.30	2.90	2.67

Using the setup in Figure 32 (b), I-V curves are obtained and plotted as shown in Figure 33 (a), with each color corresponding to contacts 1, 2, 3, 4, 6, 9, and 10. Contacts 1 and 6 were identical, so their orange and blue curves overlap. The Python code used to draw the I-V curves and extract the slope i.e., the contact resistivity, can be found Appendix A.

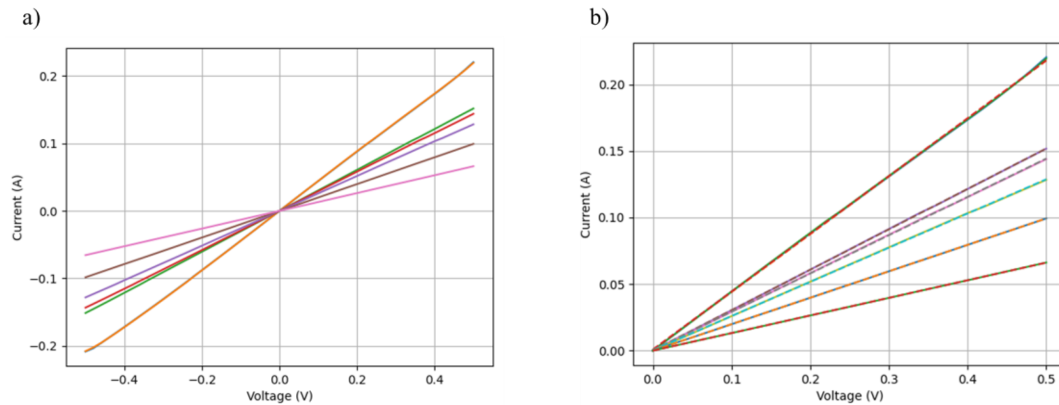

Figure 33. I-V curves of the n-Si / 1 nm thick ZrO_x / Al structure from a) -0.5 V to 0.5 V and b) 0 V to 0.5 V.

When examining only the positive region of the I-V curves, the dashed lines (slopes) in Figure 33 (b) represents the inverse of the total resistance obtained when each contact is measured ($1/R_T$). Table 6 lists the R_T for each contact, $R_T - R_S$ values, and the reciprocal of each contact's area.

Table 6. Each contact with its relative total resistance R_T obtained, $R_T - R_S$ and the reciprocal of the contact's area.

Contact #	R_T (Ω/cm)	$R_T - R_S$ (Ω/cm)	1/Area (1/cm^2)
1	2.30	1.71	10.39
2	3.29	2.15	20.37
3	3.47	1.72	31.83
4	3.89	1.75	39.30
6	2.30	1.71	10.39
9	7.56	3.35	81.49
10	5.03	2.36	49.74

Plotting R_T-R_S vs 1/area for each contact measured, Figure 34 is obtained. The trendline (the dashed line) represents the slope of the equation of straight-line discussed earlier, which represents the ρ_c. In this case, the slope is 0.021 $\Omega.cm^2$ (21 $m\Omega.cm^2$).

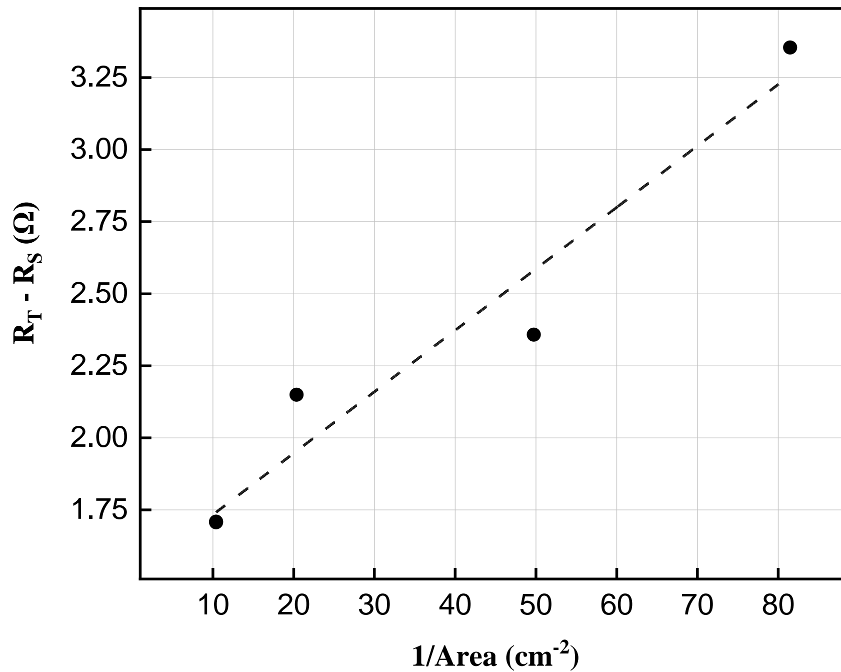

Figure 34. R_T-R_S vs the reciprocal of area for each contact. The slope of the trending-line represents the ρ_c.

Figure 35 presents the results obtained when the same procedure is applied to samples with ZrO_x thicknesses of 2, 3, 4, and 5 nm. The rest of the structure,

devices, and probes remained the same. A study reported the Al/n-Si ρ_c to be around 1000 mΩ.cm^2 [134], while another reported it to be 1216 mΩ.cm^2 [135]. Since Al/n-Si contact exhibits Schottky behavior, its ρ_c cannot be accurately found using CSM. However, another analysis called Cheung's analysis provides a more accurate ρ_c for Schottky contacts [136]. Figure 36 shows the prominent Schottky behavior of the I-V curves for Al/n-Si/Al for all contacts.

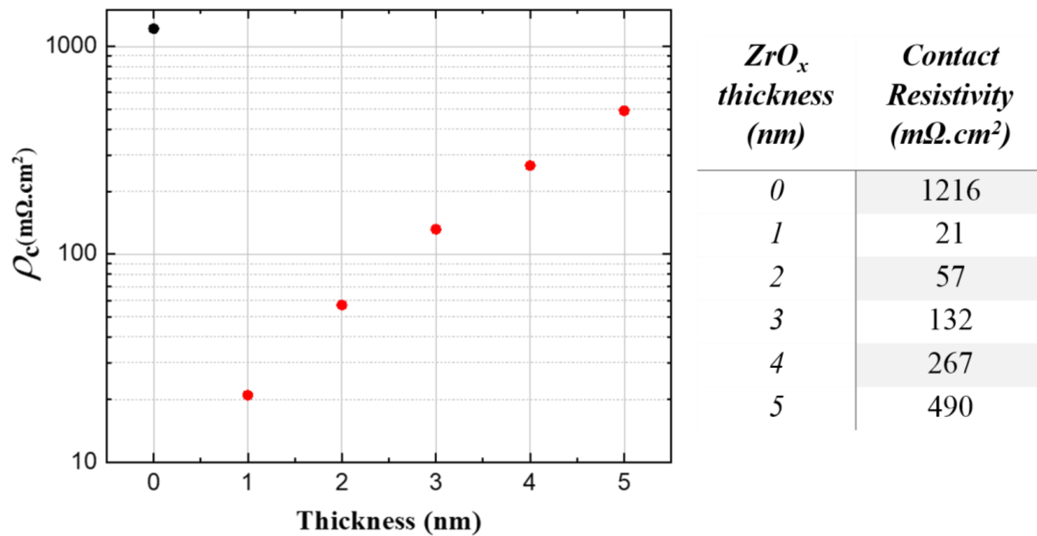

ZrO_x thickness (nm)	*Contact Resistivity (mΩ.cm^2)*
0	1216
1	21
2	57
3	132
4	267
5	490

Figure 35. Contact resistivity (ρ_c) values extracted using CSM vs the thickness of ZrO_x layer in a n-Si/Al structure.

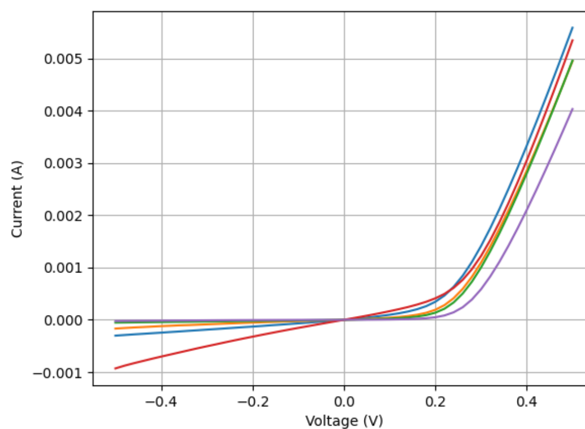

Figure 36. I-V curves for Al / n-Si / Al structure. Predominated Schottky behavior is shown.

The I-V curves show an increase in the ohmic behavior as the contact's size increases, as discussed in Chapter 2. This is because, since resistivity is a material's intrinsic property, as the size of the contact increases, its resistance decreases such that the current depends less on the rectifying contact and the whole device starts acting as a simple resistor, i.e., becomes ohmic.

CHAPTER 4

SOLAR CELL IMPLEMENTATION

4.1 n-Si in PV industry

Recently, the semiconductor electronics industry, especially PV, has been focused on working with n-Si rather than p-Si [137]. This is because n-Si wafers have a smaller number of metallic impurities (e.g., Fe) than p-Si [138]. Also, when light hits boron-doped p-Si, an undesirable interaction occurs between oxygen atoms and boron, causing recombination losses [139]. The aforementioned reasons make n-Si wafers give higher lifetimes for majority charge carriers, making them more favored than p-Si counterparts in the PV industry.

Since the rear contact area is confined in partial rear contact (PRC) solar cells, carrier recombination decreases drastically. However, this structure only works when the contact's resistivity is low enough so that charge carriers can cross the SBH using field-emission transport, as discussed in Chapter 2. Recall that the main problem regarding ρ_c is the existence of a high SBH at the MS interface.

In today's PV industry, this problem is addressed by heavily doping the rear side of the PRC solar cell with the same dopant as the active layer before metallization. For instance, for n-Si PRC solar cells, heavily doping ($N_D > 10^{21}$ atoms/cm^3) the rear side of the lightly doped ($N_D < 10^{15}$ atoms/cm^3) n-Si bulk reduces the depletion region width. This allows charge carriers to cross easily by tunneling [140], forming an ohmic contact. High doping level processes require typical temperatures above 800 °C and a high level of cleanliness, which further complicates the process [141]. Note that the SBH does not change by this method. SBH depends, primarily on the surface states, i.e., MIGS, so having a highly doped

layer passivates the dangling bonds only, which facilitates the charge carriers that tunnel through the barrier so that an ohmic behavior is observed. However, the SBH stays (almost) the same.

In the following section, an ultrathin layer of ZrO_x is used as an interlayer in an n-Si solar cell to test whether a reduction in the ρ_c and an increase in the overall efficiency of the solar cell happens.

As an interesting example, Al is used as the rear contact of the structure as it is known for its ohmic behavior with p-Si despite the significant difference between Φ_{Al} and $E_{F(p\text{-}Si)}$. One commonly accepted theory that explains the formation of p-Si/Al ohmic contact is that the positive charges in the Al are diffused into the p-Si, making a gradient in the positive charge carrier concentration along the interface [142]. This is further discussed in the following sections of this chapter.

4.2 Fabrication of a ZrO_x-Passivated n-Si Solar Cell

The first principle of designing a solar cell is to minimize the losses that could occur due to fabrication processes. The fabrication of c-Si solar cells takes place in the ODTU-GUNAM GPVL building, Ankara, Turkey. A brief description of the fabrication process of a typical c-Si solar cell is discussed below:

1. The doped as-cut silicon wafers are bought from China (Longi company).
2. KOH bath treatment for 30-45 minutes to:
    a. Remove any metallic impurities.
    b. Texture the wafer. This makes the inverted pyramid-like structure by etching all the crystallographic planes in the c-Si wafer aside from the <111> planes which allows better light capture.
3. Diffusion furnace treatment. This step is required to create the junction. The Diffusion furnace is used in doping the wafer with phosphorus (P) or boron (B). So, if the as-cut wafer is p-type, phosphorus oxychloride ($POCl_3$) gas is used to diffuse P into the wafer to make a part of its n-type, thus, creating

the junction. Diffusion occurs on both sides of the wafer, necessitating an etching process to one of the sides after this process.

4. Alumina (Al_2O_3) is deposited on the top side of the wafer by ALD.
5. SiN_x is deposited on both sides of the wafer using Plasma Enhanced Chemical Vapor Deposition (PE-CVD). SiN_x acts as an anti-reflective coating (ARC) at the top and as a capping material at the bottom. Typically, 60-80 nm of SiN_x is used for ARC purposes. This process requires great skills and knowledge because pyrophoric and toxic gases, silane and ammonia, are used under high vacuum and electric voltages. This step is what gives the solar cell its blue color.
6. Metallization processes are usually the last step. It typically occurs by ALD of Al_2O_3. Some other steps, like laser openings, might be required before metallization to allow for a better charge carrier extraction.
7. The contact metal, either Ag or Al, is thermally evaporated and deposited at the rear side of the completed structure. Screen printing of the Ag fingers is done on the top side of the structure to create the metal grid.

In this work, the zirconia layer is deposited before the metallization process using an ebeam. Then, the Al metal contact is deposited without breaking the vacuum using thermal evaporation. The final structure is schematically illustrated in Figure 37.

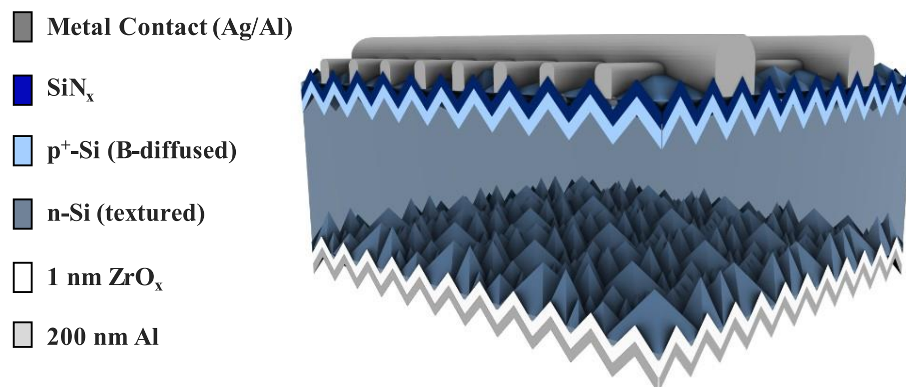

Figure 37. 3D schematic illustration of our ZrO_x passivated n-Si solar cell.

4.3 Performance of the solar cell

4.3.1 Electrical Characterization

A Newport Continuous Solar Simulator and Keithley 2400 SourceMeter characterized the fabricated solar cell schematically represented in Figure 37. The solar power is set to be 1000 W/m^2 (equivalent to 1 Sun), and the lamp is turned on at least 30 minutes before the measurement to ensure a minimum spectrum fluctuation. J-V curves are obtained by applying voltages from -0.05 V to 0.7 V throughout 221 steps, with current compliance of 250 mA (not to exceed the breakdown voltage) for the zirconia passivated solar cell. The cell's area is measured by a caliper and later corrected using EQE results, as discussed in the next section. The AM is set to 1.5. The J-V curve plotted in Figure 38 corresponds to our champion solar cell.

The 1 nm curve shows a properly functional solar cell with a relatively low series resistance and high shunt resistance. However, the 0 nm ZrO_x i.e., only Al on n-Si, shows an extremely high resistance in its structure while the 5 nm S-shaped behavior shows high series resistance. One possible explanation would be that the high thickness of the ZrO_x layer blocked all charges, not just holes. This hypothesis cannot be conformed without an extensive study and comparison of the fixed charges densities for different thicknesses of ZrO_x layers.

It is worth noting that the homogeneity and continuity of 1 nm of ZrO_x on top of a textured n-Si is questionable, to say the least. Nevertheless, it proves useful and indeed a difference in the performance of the solar cell is seen. A possible explanation would be that ZrO_x dopes the Al which make a considerable change in the workfunction of Al, ultimately, forming an ohmic contact with n-Si. However, when a 5 nm thick layer is deposited, the actual ZrO_x layer presents itself and the whole contact acts as a resistor. To summarize: 1 nm of ZrO_x forms an ohmic contact when placed between n-Si and Al while 0 nm and 5 nm do not.

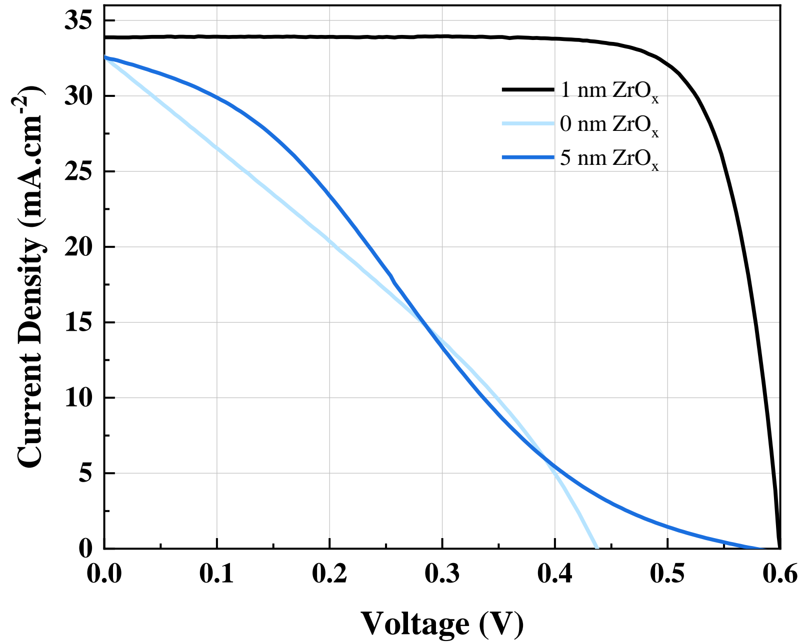

Figure 38. The J-V curve for 1 nm thick ZrO_x passivated n-Si solar cell with Al rear contact.

When the J-V curves of a solar cell are being measured, the area is required. The area is usually measured by a ruler, which could be inaccurate. In order to get the accurate area and, hence, the accurate J-V curves, a correction process is applied using EQE measurements as it gives accurate J_{SC}. Note that the J-V curves give accurate Voc and FF regardless of the area but inaccurate Jsc due to the inaccurate area.

The area of the solar cell was set to 4.6 cm^2 (inaccurate) for measuring the J-V curves using the continuous solar simulation. A $Jsc_{(4.6)}$ of 29.83 mA/cm^2 is extracted from the J-V curves. On the other hand, a $Jsc_{(EQE)}$ of 33.86 mA/cm^2 is obtained from the EQE measurements. To extract the actual (precise) area of the solar cell, the following calculation is made:

$$I_{SC} = J_{SC} \times \text{Area} = 29.83 \frac{\text{mA}}{cm^2} \times 4.6\, cm^2 = 137.2\, mA$$

$$\text{Area} = {}^{I_{SC}}/_{J_{SC}} = \frac{137.2\ mA}{33.86\ \frac{\text{mA}}{cm^2}} = 4.05\ cm^2$$

This actual area is 40.52 cm^2. To get the actual J-V curves: the $J_{4.6}$ values (at each voltage) were multiplied by the 4.6 which resulted in a list of I values. These I values were then divided by 4.05 to get the corrected J-V curves provided in Figure 38. The correction process was done for all three samples (0, 1 and 5 nm).

4.3.2 Optical Characterization

The EQE measurements were conducted by focusing a beam of light between the Ag fingers, to avoid touching the metal and losing energy from reflection on the top of the solar cell. The measurement is then carried out by changing the wavelength of that beam from 300 nm to 1200 nm by increasing 10 nm per measurement and measuring the current density (J) resulting from each change.

The EQE vs. wavelength graph for our ZrO_x incorporated n-Si solar cell and the same structure with no ZrO_x, is shown in Figure 39. The J_{SC} of the former structure (1 nm ZrO_x) and the latter structure (0 nm ZrO_x) are calculated from the curves to be 33.86 mA/cm^2 and 28.48 mA/cm^2, respectively. The improvement in the J_{SC} is over 5 mA/cm^2. In Figure 39, for all samples, the graph took an inclination at the red-light region (~700 nm), which is usually attributed to the rear surface recombination, reduced absorption at long wavelengths, and low diffusions lengths.

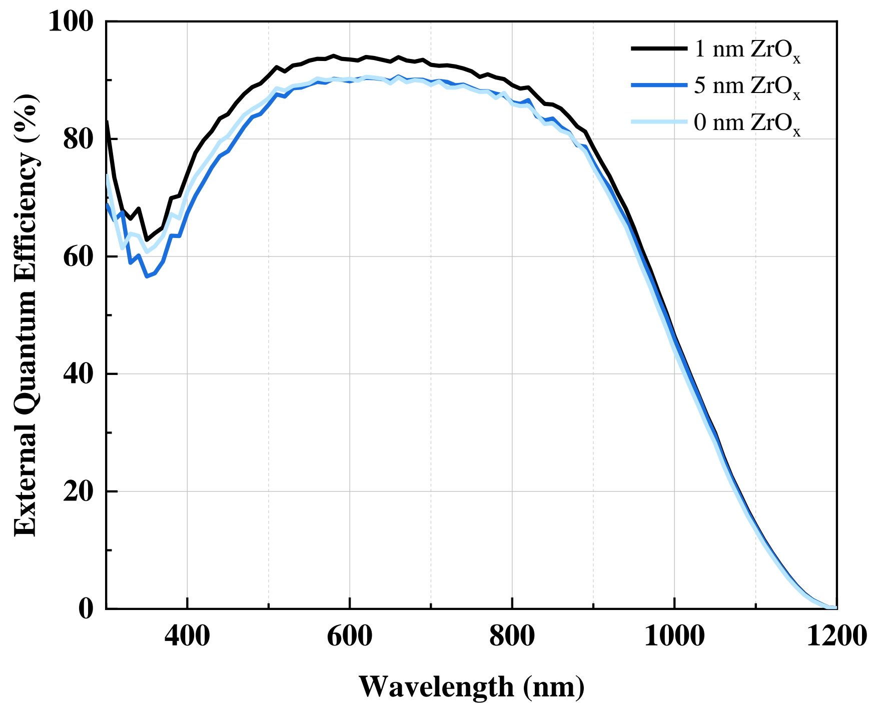

Figure 39. EQE of n-Si solar cell with a rear contact of 0, 1, and 5 nm ZrO_x with Al as a back metal contact.

The ultraviolet (UV) spectrum ranges from 100 to 400 nm, and visible light ranges from 400 to 700 nm. In c-Si solar cells, the wavelengths from 300 to 700 nm are absorbed by the top side of the solar cell and do not get past it. Since the three samples (0 nm, 1 nm, and 5 nm) were taken from the same wafer, the ultraviolet EQE behavior should be the same. However, the discrepancy observed from 400 nm to 700 nm can be attributed to the slight inhomogeneity of boron doping at the surface of the solar cell or to the slight difference in SiN_x uniformity. From 700 nm to 1000 nm, the curves behave as expected. The 1 nm sample showed an improvement in its EQE, indicating an increase in the passivation quality at the rear side. The difference between the 5 nm and 0 nm samples is negligible. Si is insensitive to wavelengths above 1000 nm. Photons in that region directly pass through it without any interaction.

In the fabricated solar cell, J_{SC} is 33.86 mA/cm^2 (338.6 A/m^2), V_{OC} is 0.6000 V, the FF is 0.791, and keeping in mind that P_{in} is 1000 W/m^2, from Eq. 7, the efficiency is,

$$\eta = \frac{0.6000\,V \times 0.791 \times 338.6\,\frac{A}{m^2}}{1000\,W/m^2} = 16.1\%$$

The V_{OC} could be further improved by annealing the structure as it is reported to "activate" the passivation properties of dielectrics by reducing the interface defect density (D_{it}) [93]. It is also highly likely that the J_{SC} will increase if the structure is annealed. Increasing the ZrO_x thickness (more than 1 nm) could also increase the V_{OC} and the J_{SC} but will surely decrease the contact resistivity of the structure, as shown from the results in Figure 35. Therefore, the optimum thickness value of the ZrO_x layer must ensure the best possible values of both the ρ_c and the V_{OC} of the solar cell.

CHAPTER 5

CONCLUSIONS AND FUTURE RECOMMENDATIONS

5.1 Conclusions

ZrO_2 uniquely features a combination of field-effect passivation, low contact resistivity values, electron-selectivity nature, stability during processing, and the ability to use ultrathin films down to 1 nm in thickness. This study also paves the way for Al to replace Ag and demonstrates the use of ZrO_x as an emerging electron-selective layer contact for n-Si wafers.

The continual increase in the concentration of greenhouse gases in the atmosphere could be lethal to life as we know it. Solar energy can replace fossil fuels as a primary energy source to prevent or decelerate further climate change.

Si solar cells' efficiencies considerably increase by the passivation of their rear contacts with a suitable material. In this work, ZrO_x was chosen as an auspicious candidate material that provides excellent passivation and acts as an electron-selective layer in c-Si solar cells by successfully depositing a 1 nm layer of ZrO_x using e-beam evaporation. Note that deposition of an ultrathin layer of ZrO_2 using solution processing techniques is a challenging endeavor.

Upon using a 1 nm-thick ZrO_x layer between the half-top structure of an n-Si solar cell and Al at the rear contact, a PCE of more than 16%, FF of more than 79%, J_{SC} of 33 mA/cm^2, and a V_{OC} of 600.0 mV were achieved.

These results are only preliminary, and there is considerable room for improvement and better results. In order to do so, some ideas are noted in the following section.

5.2 Recommendations

To improve the results obtained from the structure shown in Figure 37, calculation of the SBH (using IV or CV) should be done, followed by a calculation of the interface trap density (D_{it}) in ZrO_x. Both will provide a more significant explanation regarding the MIS structure behavior.

It is also recommended to try to deposit ZrO_2 with ALD as it has the capacity to deposit stoichiometric ZrO_2, which could increase its passivation properties, hence, increasing the V_{OC}. Deposition of less than 1 nm thick ZrO_2 between n-Si and Al using ALD could produce lower contact resistivity values.

Annealing the structure to "activate" the passivation properties of the ZrO_x layer is strongly recommended.

Laser openings might facilitate the charge carrier extraction at the rear contact.

Experiments to deposit ZrO_x on Si using HFZ with ultrasonic spray coating technique could prove helpful as this technique might be able to coat an ultrathin layer.

Finally, depositing ZrO_2 as a passivating electron-selective layer on other types of solar cells is a possible future work.

REFERENCES

[1] “Climate Change Indicators: Global Greenhouse Gas Emissions | US EPA.” https://www.epa.gov/climate-indicators/climate-change-indicators-global-greenhouse-gas-emissions (accessed Jul. 18, 2022).

[2] “World | Total including LUCF | Greenhouse Gas (GHG) Emissions | Climate Watch.” https://www.climatewatchdata.org/ghg-emissions?end_year=2019&start_year=1990 (accessed Jul. 18, 2022).

[3] “Causes of climate change | AdaptNSW.” https://www.climatechange.environment.nsw.gov.au/causes-climate-change (accessed Jul. 18, 2022).

[4] A. J. McMichael, R. E. Woodruff, and S. Hales, “Climate change and human health: present and future risks,” *Lancet*, vol. 367, no. 9513, pp. 859–869, Mar. 2006, doi: 10.1016/S0140-6736(06)68079-3.

[5] F. Cimato and M. Mullan, “Adapting to climate change: analysing the role of government,” *Defra Evidence and Analysis Series, Paper*, vol. 1, 2010.

[6] E. Outlook, “International energy outlook,” *Outlook*, 2010.

[7] T. J. Crone and M. Tolstoy, “Magnitude of the 2010 gulf of Mexico oil leak,” *Science (1979)*, vol. 330, no. 6004, p. 634, Oct. 2010, doi: 10.1126/SCIENCE.1195840/SUPPL_FILE/CRONE.SOM.PDF.

[8] H. Ritchie, M. Roser, and P. Rosado, “CO_2 and greenhouse gas emissions,” *Our world in data*, 2020.

[9] A.-E. Becquerel, “Recherches sur les effets de la radiation chimique de la lumiere solaire au moyen des courants electriques,” *CR Acad. Sci*, vol. 9, no. 145, p. 1, 1839.

[10] B. Looney, "Statistical Review of World Energy," Jul. 2021. Accessed: Jul. 19, 2022. [Online]. Available: https://www.bp.com/content/dam/bp/business-sites/en/global/corporate/pdfs/energy-economics/statistical-review/bp-stats-review-2021-full-report.pdf

[11] B. Looney, "Statistical review of world energy, 2020|," *Bp*, vol. 69, p. 66, 2020.

[12] M. Zieliński, J. Fletcher, M. Ewen, N. Fulghum, and P. Tunbridge, "Global Electricity Review 2022," Mar. 2022. Accessed: Jul. 19, 2022. [Online]. Available: https://ember-climate.org/app/uploads/2022/03/Report-GER22.pdf

[13] M. R. Hannah Ritchie and P. Rosado, "Energy," *Our World in Data*, 2020, Accessed: Jul. 19, 2022. [Online]. Available: https://ourworldindata.org/renewable-energy

[14] C. I. of T. Nathan S. Lewis and A. N. L. George Crabtree, "Basic Research Needs for Solar Energy Utilization," Renée M. Nault, Argonne National Laboratory, 2005.

[15] S. S. Hegedus and A. Luque, "Status, trends, challenges and the bright future of solar electricity from photovoltaics," *Handbook of photovoltaic science and engineering*, pp. 1–43, 2003.

[16] D. M. Chapin, C. S. Fuller, and G. L. Pearson, "A new silicon pn junction photocell for converting solar radiation into electrical power," in *Semiconductor Devices: Pioneering Papers*, World Scientific, 1991, pp. 969–970.

[17] B. G. Streetman and S. K. Banerjee, *Solid State Electronic Devices*, Seventh. Austin: Pearson, 2016.

[18] A. Zhou, Z. Yu, C. L. Chow, and D. Lau, "Enhanced solar spectral reflectance of thermal coatings through inorganic additives," *Energy Build*, vol. 138, pp. 641–647, Mar. 2017, doi: 10.1016/J.ENBUILD.2016.12.027.

[19] C. Riordan and R. Hulstron, "What is an air mass 1.5 spectrum? (solar cell performance calculations)," in *IEEE Conference on Photovoltaic Specialists*, pp. 1085–1088. doi: 10.1109/PVSC.1990.111784.

[20] A. Stjepanović, S. Stjepanović, F. Softić, and Z. Bundalo, "Microcontroller based solar tracking system," in *2009 9th International Conference on Telecommunication in Modern Satellite, Cable, and Broadcasting Services*, 2009, pp. 518–521.

[21] K. Scharf, "Photovoltaic effect produced in silicon solar cells by x-rays and gamma rays," *J Res Natl Bur Stand A Phys Chem*, vol. 64A, no. 4, p. 297, Jul. 1960, doi: 10.6028/jres.064A.029.

[22] "The Solar Spectrum And Why 'UV Solar Panels' Are A Con Job." https://www.solarquotes.com.au/blog/uv-solar-panels/ (accessed Jul. 19, 2022).

[23] K. Yoshikawa *et al.*, "Silicon heterojunction solar cell with interdigitated back contacts for a photoconversion efficiency over 26%," *Nat Energy*, vol. 2, no. 5, p. 17032, May 2017, doi: 10.1038/nenergy.2017.32.

[24] W. Shockley and H. J. Queisser, "Detailed Balance Limit of Efficiency of *p-n* Junction Solar Cells," *J Appl Phys*, vol. 32, no. 3, pp. 510–519, Mar. 1961, doi: 10.1063/1.1736034.

[25] "Best Research-Cell Efficiency Chart | Photovoltaic Research | NREL." https://www.nrel.gov/pv/cell-efficiency.html (accessed Jan. 10, 2021).

[26] T. Matsui *et al.*, "High-efficiency thin-film silicon solar cells realized by integrating stable a-Si:H absorbers into improved device design," *Jpn J Appl*

Phys, vol. 54, no. 8S1, p. 08KB10, Aug. 2015, doi: 10.7567/JJAP.54.08KB10.

[27] N. v Yastrebova, "High-efficiency multi-junction solar cells: Current status and future potential," *Centre for Research in Photonics, University of Ottawa*, p. 17, 2007.

[28] M. Kamran *et al.*, "Solar photovoltaic grid parity: a review of issues, challenges and status of different PV markets," *International Journal of Renewable Energy Research (IJRER)*, vol. 9, no. 1, pp. 244–260, 2019.

[29] H. Hoppe and N. S. Sariciftci, "Organic solar cells: An overview," *J Mater Res*, vol. 19, no. 7, pp. 1924–1945, 2004.

[30] T. Ibn-Mohammed *et al.*, "Perovskite solar cells: An integrated hybrid lifecycle assessment and review in comparison with other photovoltaic technologies," *Renewable and Sustainable Energy Reviews*, vol. 80, pp. 1321–1344, Dec. 2017, doi: 10.1016/j.rser.2017.05.095.

[31] C. B. Honsberg, R. C. Corkish, and S. P. Bremner, "A NEW GENERALIZED DETAILED BALANCE FORMULATION TO CALCULATE SOLAR CELL EFFICIENCY LIMITS".

[32] A. de Vos and H. Pauwels, "On the thermodynamic limit of photovoltaic energy conversion," *Applied physics*, vol. 25, no. 2, pp. 119–125, Jun. 1981, doi: 10.1007/BF00901283.

[33] M. A. Green, E. D. Dunlop, J. Hohl-Ebinger, M. Yoshita, N. Kopidakis, and X. Hao, "Solar cell efficiency tables (Version 58)," *Progress in Photovoltaics: Research and Applications*, vol. 29, no. 7, pp. 657–667, Jul. 2021, doi: 10.1002/pip.3444.

[34] M. M. Moslehi *et al.*, "World-record 20.6% efficiency 156 mm x 156 mm full-square solar cells using low-cost kerfless ultrathin epitaxial silicon & porous silicon lift-off technology for industry-leading high-performance

smart PV modules," in *PV Asia Pacific Conference (APVIA/PVAP)*, 2012, vol. 24.

[35] M. J. Keevers, T. L. Young, U. Schubert, and M. A. Green, "10% efficient CSG minimodules," in *22nd European Photovoltaic Solar Energy Conference*, 2007, vol. 3, no. September, pp. 1783–1790.

[36] B. M. Kayes *et al.*, "27.6% conversion efficiency, a new record for single-junction solar cells under 1 sun illumination," in *2011 37th IEEE Photovoltaic Specialists Conference*, 2011, pp. 4–8.

[37] M. Wanlass, "Systems and methods for advanced ultra-high-performance InP solar cells," National Renewable Energy Lab.(NREL), Golden, CO (United States), 2017.

[38] M. Nakamura, K. Yamaguchi, Y. Kimoto, Y. Yasaki, T. Kato, and H. Sugimoto, "Cd-free Cu (In, Ga)(Se, S) 2 thin-film solar cell with record efficiency of 23.35%," *IEEE J Photovolt*, vol. 9, no. 6, pp. 1863–1867, 2019.

[39] F. Solar, "First Solar builds the highest efficiency thin film PV cell on record," *First Solar*, vol. 5, 2014.

[40] C. Yan *et al.*, "Cu2ZnSnS4 solar cells with over 10% power conversion efficiency enabled by heterojunction heat treatment," *Nat Energy*, vol. 3, no. 9, pp. 764–772, 2018.

[41] T. Matsui *et al.*, "High-efficiency amorphous silicon solar cells: Impact of deposition rate on metastability," *Appl Phys Lett*, vol. 106, no. 5, p. 053901, 2015.

[42] H. Sai, T. Matsui, H. Kumagai, and K. Matsubara, "Thin-film microcrystalline silicon solar cells: 11.9% efficiency and beyond," *Applied Physics Express*, vol. 11, no. 2, p. 022301, 2018.

[43] J. Peng *et al.*, “Nanoscale localized contacts for high fill factors in polymer-passivated perovskite solar cells,” *Science (1979)*, vol. 371, no. 6527, pp. 390–395, 2021.

[44] P. Liu, G. Tang, and F. Yan, “Strategies for Large-Scale Fabrication of Perovskite Films for Solar Cells,” *Solar RRL*, vol. 6, no. 1, p. 2100683, 2022.

[45] R. Komiya, A. Fukui, N. Murofushi, N. Koide, R. Yamanaka, and H. Katayama, “Improvement of the conversion efficiency of a monolithic type dye-sensitized solar cell module,” in *Technical Digest, 21st International Photovoltaic Science and Engineering Conference*, 2011, vol. 2.

[46] K. O. Brinkmann *et al.*, “The Optical Origin of Near-Unity External Quantum Efficiencies in Perovskite Solar Cells,” *Solar RRL*, vol. 5, no. 9, p. 2100371, Sep. 2021, doi: 10.1002/solr.202100371.

[47] D. Timmerman, I. Izeddin, P. Stallinga, I. N. Yassievich, and T. Gregorkiewicz, “Space-separated quantum cutting with silicon nanocrystals for photovoltaic applications,” *Nat Photonics*, vol. 2, no. 2, pp. 105–109, Feb. 2008, doi: 10.1038/nphoton.2007.279.

[48] E. Radziemska, “The effect of temperature on the power drop in crystalline silicon solar cells,” *Renew Energy*, vol. 28, no. 1, pp. 1–12, Jan. 2003, doi: 10.1016/S0960-1481(02)00015-0.

[49] D. S. Kim, S. G. Yoon, G. E. Jang, S. J. Suh, H. Kim, and D. H. Yoon, “Refractive index properties of SiN thin films and fabrication of SiN optical waveguide,” *J Electroceram*, vol. 17, no. 2–4, pp. 315–318, Dec. 2006, doi: 10.1007/s10832-006-9710-x.

[50] E. Yablonovich and G. D. Cody, “Intensity Enhancement in Textured Optical Sheets for Solar Cells,” *IEEE Trans Electron Devices*, vol. ED-29, pp. 300–305, 1982.

[51] D. A. Jacobs, K. R. Catchpole, F. J. Beck, and T. P. White, "A re-evaluation of transparent conductor requirements for thin-film solar cells," *J Mater Chem A Mater*, vol. 4, no. 12, pp. 4490–4496, Mar. 2016, doi: 10.1039/C6TA01670G.

[52] W. Shockley and W. T. Read Jr, "Statistics of the recombinations of holes and electrons," *Physical review*, vol. 87, no. 5, p. 835, 1952.

[53] R. N. Hall, "Electron-hole recombination in germanium," *Physical review*, vol. 87, no. 2, p. 387, 1952.

[54] K. Oura, V. G. Lifshits, A. A. Saranin, A. v Zotov, and M. Katayama, *Surface science: an introduction*. Springer Science & Business Media, 2013.

[55] A. Richter, F. Werner, A. Cuevas, J. Schmidt, and S. W. Glunz, "Improved Parameterization of Auger Recombination in Silicon," *Energy Procedia*, vol. 27, pp. 88–94, 2012, doi: 10.1016/j.egypro.2012.07.034.

[56] A. Reinders, P. Verlinden, W. van Sark, and A. Freundlich, *Photovoltaic solar energy: from fundamentals to applications*. John Wiley & Sons, 2017.

[57] W. Soppe, H. Rieffe, and A. Weeber, "Bulk and surface passivation of silicon solar cells accomplished by silicon nitride deposited on industrial scale by microwave PECVD," *Progress in Photovoltaics: Research and Applications*, vol. 13, no. 7, pp. 551–569, Nov. 2005, doi: 10.1002/PIP.611.

[58] A. G. Aberle, "Overview on SiN surface passivation of crystalline silicon solar cells," *Solar Energy Materials and Solar Cells*, vol. 65, no. 1–4, pp. 239–248, Jan. 2001, doi: 10.1016/S0927-0248(00)00099-4.

[59] J. Schmidt and A. G. Aberle, "Carrier recombination at silicon–silicon nitride interfaces fabricated by plasma-enhanced chemical vapor deposition," *J Appl Phys*, vol. 85, no. 7, p. 3626, Mar. 1999, doi: 10.1063/1.369725.

[60] S. Rein, *Lifetime spectroscopy: a method of defect characterization in silicon for photovoltaic applications*, vol. 85. Springer Science & Business Media, 2006.

[61] Y. Larionova, V. Mertens, N.-P. Harder, and R. Brendel, "Surface passivation of n-type Czochralski silicon substrates by thermal-SiO2/plasma-enhanced chemical vapor deposition SiN stacks," *Appl Phys Lett*, vol. 96, no. 3, p. 032105, Jan. 2010, doi: 10.1063/1.3291681.

[62] G. Dingemans, N. M. Terlinden, M. A. Verheijen, M. C. M. van de Sanden, and W. M. M. Kessels, "Controlling the fixed charge and passivation properties of Si(100)/Al_2O_3 interfaces using ultrathin SiO_2 interlayers synthesized by atomic layer deposition," *J Appl Phys*, vol. 110, no. 9, p. 093715, Nov. 2011, doi: 10.1063/1.3658246.

[63] G. Agostinelli *et al.*, "Very low surface recombination velocities on p-type silicon wafers passivated with a dielectric with fixed negative charge," *Solar Energy Materials and Solar Cells*, vol. 90, no. 18–19, pp. 3438–3443, Nov. 2006, doi: 10.1016/j.solmat.2006.04.014.

[64] B. Hoex, S. B. S. Heil, E. Langereis, M. C. M. van de Sanden, and W. M. M. Kessels, "Ultralow surface recombination of c-Si substrates passivated by plasma-assisted atomic layer deposited Al2O3," *Appl Phys Lett*, vol. 89, no. 4, p. 042112, Jul. 2006, doi: 10.1063/1.2240736.

[65] D. Pysch *et al.*, "IMPLEMENTATION OF AN ALD-AL2O3 PERC-TECHNOLOGY INTO A MULTI-AND MONOCRYSTALLINE INDUSTRIAL PILOT PRODUCTION Ultra lightweight PV modules and their applications in innovative PV systems achieving lowest LCOE View project2 SUBJECT 2.2 Silicon Solar Cell Improvements IMPLEMENTATION OF AN ALD-AL 2 O 3 PERC-TECHNOLOGY INTO A MULTI-AND MONOCRYSTALLINE INDUSTRIAL PILOT

PRODUCTION”, Accessed: Jul. 20, 2022. [Online]. Available: https://www.researchgate.net/publication/273341418

[66] W. M. M. Kessels and R. Brendel, “Progress in the surface passivation of silicon solar cells,” 2008, Accessed: Jul. 20, 2022. [Online]. Available: www.tue.nl/taverne

[67] J.-W. A. Schüttauf, K. H. M. van der Werf, I. M. Kielen, W. G. J. H. M. van Sark, J. K. Rath, and R. E. I. Schropp, “High quality crystalline silicon surface passivation by combined intrinsic and n-type hydrogenated amorphous silicon,” *Appl Phys Lett*, vol. 99, no. 20, p. 203503, Nov. 2011, doi: 10.1063/1.3662404.

[68] M. Hofmann *et al.*, “Recent developments in rear-surface passivation at Fraunhofer ISE,” *Solar Energy Materials and Solar Cells*, vol. 93, no. 6–7, pp. 1074–1078, Jun. 2009, doi: 10.1016/j.solmat.2008.11.056.

[69] M. Hofmann, C. Schmidt, N. Kohn, J. Rentsch, S. W. Glunz, and R. Preu, “Stack system of PECVD amorphous silicon and PECVD silicon oxide for silicon solar cell rear side passivation,” *Progress in Photovoltaics: Research and Applications*, vol. 16, no. 6, pp. 509–518, Sep. 2008, doi: 10.1002/pip.835.

[70] S. Olibet, E. Vallat-Sauvain, C. Ballif, L. Korte, and L. Fesquet, “Silicon solar cell passivation using heterostructures,” 2007.

[71] M. J. Kerr and A. Cuevas, “Very low bulk and surface recombination in oxidized silicon wafers,” *Semicond Sci Technol*, vol. 17, no. 1, pp. 35–38, Jan. 2002, doi: 10.1088/0268-1242/17/1/306.

[72] X. Yang *et al.*, “Atomic Layer Deposition of Vanadium Oxide as Hole-Selective Contact for Crystalline Silicon Solar Cells,” *Adv Electron Mater*, vol. 6, no. 8, p. 2000467, Aug. 2020, doi: 10.1002/aelm.202000467.

[73] K. A. Nagamatsu *et al.*, “Titanium dioxide/silicon hole-blocking selective contact to enable double-heterojunction crystalline silicon-based solar cell,” *Appl Phys Lett*, vol. 106, no. 12, p. 123906, Mar. 2015, doi: 10.1063/1.4916540.

[74] Y. Wan *et al.*, “Tantalum Oxide Electron-Selective Heterocontacts for Silicon Photovoltaics and Photoelectrochemical Water Reduction,” *ACS Energy Lett*, vol. 3, no. 1, pp. 125–131, Jan. 2018, doi: 10.1021/acsenergylett.7b01153.

[75] B. Macco *et al.*, “Atomic-layer deposited Nb2O5 as transparent passivating electron contact for c-Si solar cells,” *Solar Energy Materials and Solar Cells*, vol. 184, pp. 98–104, Sep. 2018, doi: 10.1016/j.solmat.2018.04.037.

[76] X. Yang *et al.*, “Tantalum Nitride Electron-Selective Contact for Crystalline Silicon Solar Cells,” *Adv Energy Mater*, vol. 8, no. 20, p. 1800608, Jul. 2018, doi: 10.1002/aenm.201800608.

[77] J. Yu *et al.*, “Titanium Nitride Electron-Conductive Contact for Silicon Solar Cells By Radio Frequency Sputtering from a TiN Target,” *ACS Appl Mater Interfaces*, vol. 12, no. 23, pp. 26177–26183, Jun. 2020, doi: 10.1021/acsami.0c04439.

[78] B. Chen *et al.*, “Magnesium thin film as a doping-free back surface field layer for hybrid solar cells,” *Appl Phys Lett*, vol. 110, no. 13, p. 133504, Mar. 2017, doi: 10.1063/1.4979345.

[79] Y. Wan *et al.*, “Magnesium Fluoride Electron-Selective Contacts for Crystalline Silicon Solar Cells,” *ACS Appl Mater Interfaces*, vol. 8, no. 23, pp. 14671–14677, Jun. 2016, doi: 10.1021/acsami.6b03599.

[80] J. Kang *et al.*, “Electron-Selective Lithium Contacts for Crystalline Silicon Solar Cells,” *Adv Mater Interfaces*, vol. 8, no. 12, p. 2100015, Jun. 2021, doi: 10.1002/admi.202100015.

[81] J. Bullock *et al.*, "Efficient silicon solar cells with dopant-free asymmetric heterocontacts," *Nat Energy*, vol. 1, no. 3, p. 15031, Mar. 2016, doi: 10.1038/nenergy.2015.31.

[82] J. Bullock, A. Cuevas, T. Allen, and C. Battaglia, "Molybdenum oxide MoO $_x$: A versatile hole contact for silicon solar cells," *Appl Phys Lett*, vol. 105, no. 23, p. 232109, Dec. 2014, doi: 10.1063/1.4903467.

[83] M. Bivour, B. Macco, J. Temmler, W. M. M. (Erwin) Kessels, and M. Hermle, "Atomic Layer Deposited Molybdenum Oxide for the Hole-selective Contact of Silicon Solar Cells," *Energy Procedia*, vol. 92, pp. 443–449, Aug. 2016, doi: 10.1016/j.egypro.2016.07.125.

[84] B. Macco, M. F. J. Vos, N. F. W. Thissen, A. A. Bol, and W. M. M. Kessels, "Low-temperature atomic layer deposition of MoO $_x$ for silicon heterojunction solar cells," *physica status solidi (RRL) - Rapid Research Letters*, vol. 9, no. 7, pp. 393–396, Jul. 2015, doi: 10.1002/pssr.201510117.

[85] M. Bivour, J. Temmler, H. Steinkemper, and M. Hermle, "Molybdenum and tungsten oxide: High work function wide band gap contact materials for hole selective contacts of silicon solar cells," *Solar Energy Materials and Solar Cells*, vol. 142, pp. 34–41, Nov. 2015, doi: 10.1016/j.solmat.2015.05.031.

[86] J. Sheng *et al.*, "Improvement of the SiO $_x$ Passivation Layer for High-Efficiency Si/PEDOT:PSS Heterojunction Solar Cells," *ACS Appl Mater Interfaces*, vol. 6, no. 18, pp. 16027–16034, Sep. 2014, doi: 10.1021/am503949g.

[87] M.-U. Halbich, D. Zielke, R. Gogolin, R. Sauer-Stieglitz, W. Lövenich, and J. Schmidt, "Improved surface passivation and reduced parasitic absorption in PEDOT:PSS/c-Si heterojunction solar cells through the admixture of sorbitol," *Sci Rep*, vol. 9, no. 1, p. 9775, Dec. 2019, doi: 10.1038/s41598-019-46280-y.

[88] S. W. Glunz and F. Feldmann, "SiO2 surface passivation layers – a key technology for silicon solar cells," *Solar Energy Materials and Solar Cells*, vol. 185, pp. 260–269, Oct. 2018, doi: 10.1016/j.solmat.2018.04.029.

[89] M. R. Baklanov, M. L. Green, and K. Maex, *Dielectric Films for Advanced Microelectronics*. Chichester, UK: John Wiley & Sons, Ltd, 2007. doi: 10.1002/9780470017944.

[90] J. He *et al.*, "Stable Electron-Selective Contacts for Crystalline Silicon Solar Cells Enabling Efficiency over 21.6%," *Adv Funct Mater*, vol. 30, no. 50, p. 2005554, Dec. 2020, doi: 10.1002/adfm.202005554.

[91] M. Vasilopoulou *et al.*, "Atomic layer deposited zirconium oxide electron injection layer for efficient organic light emitting diodes," *Org Electron*, vol. 14, no. 1, pp. 312–319, Jan. 2013, doi: 10.1016/j.orgel.2012.10.006.

[92] N. Tokmoldin, N. Griffiths, D. D. C. Bradley, and S. A. Haque, "A Hybrid Inorganic-Organic Semiconductor Light-Emitting Diode Using ZrO_2 as an Electron-Injection Layer," *Advanced Materials*, vol. 21, no. 34, pp. 3475–3478, Sep. 2009, doi: 10.1002/adma.200802594.

[93] Y. Wan *et al.*, "Zirconium oxide surface passivation of crystalline silicon," *Appl Phys Lett*, vol. 112, no. 20, p. 201604, May 2018, doi: 10.1063/1.5032226.

[94] Y. H. Wong and K. Y. Cheong, "ZrO2 thin films on Si substrate," *Journal of Materials Science: Materials in Electronics*, vol. 21, no. 10, pp. 980–993, Oct. 2010, doi: 10.1007/s10854-010-0144-5.

[95] T. S. Jeon, J. M. White, and D. L. Kwong, "Thermal stability of ultrathin ZrO 2 films prepared by chemical vapor deposition on Si (100)," *Appl Phys Lett*, vol. 78, no. 3, pp. 368–370, 2001.

[96] M. A. Gribelyuk, A. Callegari, E. P. Gusev, M. Copel, and D. A. Buchanan, “Interface reactions in ZrO 2 based gate dielectric stacks,” *J Appl Phys*, vol. 92, no. 3, pp. 1232–1237, 2002.

[97] H. S. Choi, K. S. Seol, J. S. Kwak, C.-S. Son, and I.-H. Choi, “Thermal treatment effects on interfacial layer formation between ZrO2 thin films and Si substrates,” *Vacuum*, vol. 80, no. 4, pp. 310–316, 2005.

[98] X. Wu, D. Landheer, M. J. Graham, H.-W. Chen, T.-Y. Huang, and T.-S. Chao, “Structure and thermal stability of MOCVD ZrO2 films on Si (1 0 0),” *J Cryst Growth*, vol. 250, no. 3–4, pp. 479–485, 2003.

[99] S. Venkataraj, O. Kappertz, C. Liesch, R. Detemple, R. Jayavel, and M. Wuttig, “Thermal stability of sputtered zirconium oxide films,” *Vacuum*, vol. 75, no. 1, pp. 7–16, 2004.

[100] E. v Stefanovich, A. L. Shluger, and C. R. A. Catlow, “Theoretical study of the stabilization of cubic-phase Zr02 by impurities,” *Phys Rev B*, vol. 49, 1994.

[101] M. Yoshimura, “Phase stability of zirconia,” *Am. Ceram. Soc. Bull.;(United States)*, vol. 67, no. 12, 1988.

[102] Y. H. Wong and K. Y. Cheong, “Band alignment and enhanced breakdown field of simultaneously oxidized and nitrided Zr film on Si,” *Nanoscale Res Lett*, vol. 6, no. 1, pp. 1–5, Aug. 2011, doi: 10.1186/1556-276X-6-489/FIGURES/4.

[103] B. Králik, E. K. Chang, and S. G. Louie, “Structural properties and quasiparticle band structure of zirconia,” *Phys Rev B*, vol. 57, no. 12, pp. 7027–7036, Mar. 1998, doi: 10.1103/PhysRevB.57.7027.

[104] S. Venkataraj, O. Kappertz, H. Weis, R. Drese, R. Jayavel, and M. Wuttig, “Structural and optical properties of thin zirconium oxide films prepared by

reactive direct current magnetron sputtering," *J Appl Phys*, vol. 92, no. 7, pp. 3599–3607, Oct. 2002, doi: 10.1063/1.1503858.

[105] L. S. Hung, C. W. Tang, and M. G. Mason, "Enhanced electron injection in organic electroluminescence devices using an Al/LiF electrode," *Appl Phys Lett*, vol. 70, no. 2, pp. 152–154, Jan. 1997, doi: 10.1063/1.118344.

[106] C. Ganzorig, K. Suga, and M. Fujihira, "Alkali metal acetates as effective electron injection layers for organic electroluminescent devices," *Materials Science and Engineering: B*, vol. 85, no. 2–3, pp. 140–143, Aug. 2001, doi: 10.1016/S0921-5107(01)00547-5.

[107] C. J. Brabec, S. E. Shaheen, C. Winder, N. S. Sariciftci, and P. Denk, "Effect of LiF/metal electrodes on the performance of plastic solar cells," *Appl Phys Lett*, vol. 80, no. 7, pp. 1288–1290, Feb. 2002, doi: 10.1063/1.1446988.

[108] S. E. Shaheen *et al.*, "Bright blue organic light-emitting diode with improved color purity using a LiF/Al cathode," *J Appl Phys*, vol. 84, no. 4, pp. 2324–2327, Aug. 1998, doi: 10.1063/1.368299.

[109] "Fundamentals of Semiconductor physics - Energy Bands." http://www.optique-ingenieur.org/en/courses/OPI_ang_M05_C02/co/Contenu.html (accessed Jul. 29, 2022).

[110] W. Schottky, "Halbleitertheorie der Sperrschicht," *Naturwissenschaften 1938 26:52*, vol. 26, no. 52, pp. 843–843, Dec. 1938, doi: 10.1007/BF01774216.

[111] S. Park *et al.*, "The Schottky–Mott Rule Expanded for Two-Dimensional Semiconductors: Influence of Substrate Dielectric Screening," *ACS Nano*, vol. 15, no. 9, pp. 14794–14803, Sep. 2021, doi: 10.1021/acsnano.1c04825.

[112] I. P. Vali, P. K. Shetty, M. G. Mahesha, V. C. Petwal, J. Dwivedi, and R. J. Choudhary, "Tuning of Schottky barrier height of Al/n-Si by electron beam

irradiation," *Appl Surf Sci*, vol. 407, pp. 171–176, Jun. 2017, doi: 10.1016/j.apsusc.2017.02.189.

[113] J. Bardeen, "Surface States and Rectification at a Metal Semi-Conductor Contact," *Physical Review*, vol. 71, no. 10, p. 717, May 1947, doi: 10.1103/PhysRev.71.717.

[114] S. Grover, "Effect of Transmission Line Measurement (TLM) Geometry on Effect of Transmission Line Measurement (TLM) Geometry on Specific Contact Resistivity Determination Specific Contact Resistivity Determination," 2016, Accessed: Aug. 11, 2022. [Online]. Available: https://scholarworks.rit.edu/theses

[115] A. M. Cowley and S. M. Sze, "Surface States and Barrier Height of Metal-Semiconductor Systems," *J Appl Phys*, vol. 36, no. 10, pp. 3212–3220, Oct. 1965, doi: 10.1063/1.1702952.

[116] R. P. Gupta, J. B. White, O. D. Iyore, U. Chakrabarti, H. N. Alshareef, and B. E. Gnade, "Determination of Contact Resistivity by the Cox and Strack Method for Metal Contacts to Bulk Bismuth Antimony Telluride," 2009, doi: 10.1149/1.3143918.

[117] M. van Rijnbach, R. J. E. Hueting, M. Stodolny, G. Janssen, J. Melskens, and J. Schmitz, "On the Accuracy of the Cox–Strack Equation and Method for Contact Resistivity Determination," *IEEE Trans Electron Devices*, vol. 67, no. 4, pp. 1757–1763, Apr. 2020, doi: 10.1109/TED.2020.2974194.

[118] I. Ben Miled *et al.*, "Structural, optical, and electrical properties of cadmium oxide thin films prepared by sol–gel spin-coating method," *J Solgel Sci Technol*, vol. 83, no. 2, pp. 259–267, Aug. 2017, doi: 10.1007/s10971-017-4412-1.

[119] D. J. Estes and M. Mayer, "Electroformation of giant liposomes from spin-coated films of lipids," *Colloids Surf B Biointerfaces*, vol. 42, no. 2, pp. 115–123, May 2005, doi: 10.1016/j.colsurfb.2005.01.016.

[120] "BONDERITE M-NT 1," 2016.

[121] M. Maczka *et al.*, "Spectroscopic studies of dynamically compacted monoclinic ZrO2," *Journal of Physics and Chemistry of Solids*, vol. 60, no. 12, pp. 1909–1914, Dec. 1999, doi: 10.1016/S0022-3697(99)00221-8.

[122] M. Shane and M. L. Mecartney, "Sol-gel synthesis of zirconia barrier coatings".

[123] A. A. Abrashov, N. S. Grigoryan, T. A. Vagramyan, V. P. Meshalkin, A. V. Kotel'nikova, and A. A. Gribanova, "Protective adhesive zirconium oxide coatings," *Protection of Metals and Physical Chemistry of Surfaces*, vol. 52, no. 7, pp. 1170–1174, Dec. 2016, doi: 10.1134/S2070205116070029.

[124] P. O. Oviroh, R. Akbarzadeh, D. Pan, R. A. M. Coetzee, and T.-C. Jen, "New development of atomic layer deposition: processes, methods and applications," *Sci Technol Adv Mater*, vol. 20, no. 1, pp. 465–496, Dec. 2019, doi: 10.1080/14686996.2019.1599694.

[125] X. Wang *et al.*, "Atomic layer deposition of zirconium oxide thin films," *J Mater Res*, vol. 35, no. 7, pp. 804–812, Apr. 2020, doi: 10.1557/jmr.2019.338.

[126] R. H. J. Vervuurt, W. M. M. E. Kessels, and A. A. Bol, "Atomic Layer Deposition for Graphene Device Integration," *Adv Mater Interfaces*, vol. 4, no. 18, p. 1700232, Sep. 2017, doi: 10.1002/admi.201700232.

[127] L. Sygellou *et al.*, "ZrO2 and Al2O3 Thin Films on Ge(100) Grown by ALD: An XPS Investigation," *Surface Science Spectra*, vol. 18, no. 1, pp. 58–67, Dec. 2011, doi: 10.1116/11.20100901.

[128] C. O. de González and E. A. García, "An X-ray photoelectron spectroscopy study of the surface oxidation of zirconium," *Surf Sci*, vol. 193, no. 3, pp. 305–320, Jan. 1988, doi: 10.1016/0039-6028(88)90438-4.

[129] "Kurt J. Lesker Company | Zirconium Oxide ZrO2 Pieces Evaporation Materials | Vacuum Science Is Our Business." https://www.lesker.com/newweb/deposition_materials/depositionmaterials_evaporationmaterials_1.cfm?pgid=zr2 (accessed Jan. 17, 2022).

[130] "Kurt J. Lesker Company | Zirconium Zr Evaporation Process Notes | Vacuum Science Is Our Business." https://www.lesker.com/newweb/deposition_materials/deposition-materials-notes.cfm?pgid=zr1 (accessed Jan. 17, 2022).

[131] J. Li, S. Meng, J. Niu, and H. Lu, "Electronic structures and optical properties of monoclinic ZrO 2 studied by first-principles local density approximation + U approach," *Journal of Advanced Ceramics*, vol. 6, no. 1, pp. 43–49, 2017, doi: 10.1007/s40145-016-0216-y.

[132] D. Barreca, G. A. Battiston, R. Gerbasi, E. Tondello, and P. Zanella, "Zirconium Dioxide Thin Films Characterized by XPS," *Surface Science Spectra*, vol. 7, no. 4, pp. 303–309, Oct. 2000, doi: 10.1116/1.1375573.

[133] W. Kern, "The Evolution of Silicon Wafer Cleaning Technology," *J Electrochem Soc*, vol. 137, no. 6, pp. 1887–1892, Jun. 1990, doi: 10.1149/1.2086825.

[134] X. Yang, Q. Bi, H. Ali, K. Davis, W. v. Schoenfeld, and K. Weber, "High-Performance TiO_2-Based Electron-Selective Contacts for Crystalline Silicon Solar Cells," *Advanced Materials*, vol. 28, no. 28, pp. 5891–5897, Jul. 2016, doi: 10.1002/adma.201600926.

[135] L. Yao *et al.*, "Solution-processed and annealing-free zirconium acetylacetonate electron-selective contacts for efficient crystalline silicon solar cells," *Solar Energy*, vol. 215, pp. 410–415, Feb. 2021, doi: 10.1016/j.solener.2020.12.048.

[136] S. K. Cheung and N. W. Cheung, “Extraction of Schottky diode parameters from forward current-voltage characteristics,” *Appl Phys Lett*, vol. 49, no. 2, pp. 85–87, Jul. 1986, doi: 10.1063/1.97359.

[137] A. Metz, M. Fischer, and J. Trube, “Recent Results of the International Technology Roadmap for Photovoltaics (ITRPV),” Sydney, Mar. 2017.

[138] A. Richter, J. Benick, A. Fell, M. Hermle, and S. W. Glunz, “Impact of bulk impurity contamination on the performance of high-efficiency *n* -type silicon solar cells,” *Progress in Photovoltaics: Research and Applications*, vol. 26, no. 5, pp. 342–350, May 2018, doi: 10.1002/pip.2990.

[139] J. Schmidt and A. Cuevas, “Electronic properties of light-induced recombination centers in boron-doped Czochralski silicon,” *J Appl Phys*, vol. 86, no. 6, pp. 3175–3180, Sep. 1999, doi: 10.1063/1.371186.

[140] J. Benick, B. Hoex, M. C. M. van de Sanden, W. M. M. Kessels, O. Schultz, and S. W. Glunz, “High efficiency n-type Si solar cells on Al2O3-passivated boron emitters,” *Appl Phys Lett*, vol. 92, no. 25, p. 253504, Jun. 2008, doi: 10.1063/1.2945287.

[141] S. W. Glunz, R. Preu, and D. Biro, “Crystalline Silicon Solar Cells,” in *Comprehensive Renewable Energy*, Elsevier, 2012, pp. 353–387. doi: 10.1016/B978-0-08-087872-0.00117-7.

[142] M. Siad, A. Keffous, S. Mamma, Y. Belkacem, and H. Menari, “Correlation between series resistance and parameters of Al/n-Si and Al/p-Si Schottky barrier diodes,” *Appl Surf Sci*, vol. 236, no. 1–4, pp. 366–376, Sep. 2004, doi: 10.1016/J.APSUSC.2004.05.009.

APPENDICES

A. Appendix A

```
import matplotlib.pyplot as pl
import numpy as np
import math as ma


def ohm(a,
        npt):

    data = open(a, 'r')
    arr = data.read().split('\n') #

    list = []
    for n in arr:
        list.append(n.split('\t'))
    list.pop()

    voltx = []
    currx = []
    for n in list: #n is line
        voltx.append(float((n[0]))) .
        currx.append(float((n[1])))

    volt = [] .
    curr = []
    if str(npt) == 'n':
        for n in range(len(voltx)):

            if voltx[n] <= 0:
                volt.append(voltx[n])
                curr.append(currx[n])
    if str(npt) == 'p':
        for n in range(len(voltx)):
            if voltx[n] >= 0:
                volt.append(voltx[n])
                curr.append(currx[n])
    if str(npt) == 't':
        for n in range(len(voltx)):
            volt.append(voltx[n])
            curr.append(currx[n])

    slope, intercept = np.polyfit(volt, curr, 1)

    print('Slope:', slope, 'Intercept:', intercept)

    y = []
    for n in volt:
        v = slope * n + intercept
        y.append(v)
```

```
    pl.plot(volt, curr)
    pl.plot(volt,y,'--')

    pl.xlabel('Voltage (V)')
    pl.ylabel('Current (A)')
    pl.grid(1)

    return (slope)  # slope is 1/R_t


def rtfunc(x):  # Finds R_t value
    y = []
    for n in range(len(x)):
        xn = (1 / x[n])
        y.append(xn)
    return (y)


def rsfunc(p, d, t, on):

    rs = []
    if str(on) == 'o':
        for n in d:
            b = (2 / pi) * ma.atan((4 * t) / n)
            rsn = p / (2 * n) * b
            rs.append(rsn)
    if str(on) == 'n':
        for n in d:
            b = (4 / pi) * (n / (2 * t) + 4 / pi + (1 - 4 / pi) *
ma.atan(2 * n / (3 * t))) ** (-1)
            rsn = p / (2 * n) * b
            rs.append(rsn)
    return (rs)


def lastplot(c, r):
    slope, intercept = np.polyfit((c), (r), 1)
    print('Final slope = ', slope)
    print('Final intercept =', intercept)

    y = []
    for n in c:
        v = slope * n + intercept
        y.append(v)

    pl.cla()

    pl.plot(c, r, 'bo')
    pl.plot(c, y, '--')

    pl.xlabel('1/Area (cm-2)')
    pl.ylabel('Rt - Rs (OHM)')
    pl.grid(1)
```

```
    pl.show()              #Final plot of Rt - Rs vs 1/Area (If you
want to use this, remove the # in the beginning and add # to the
beginning of line 133)


npt = 'p'  # which side of voltage do you want to consider?
(negative voltage : 'n'), ( positive : 'p'), (all : 't')
on = 'o'  # which B (geometrical factor in R_s) do you want to use?
(old cox-strack : 'o'), (new Rijnbach : 'n')

rr = [  # only change the values between quotes. list the data
texts from the ones with larger diameters to smaller.
    ohm('1.txt', npt),
    ohm('6.txt', npt),
    ohm('2.txt', npt),
    ohm('3.txt', npt),
    ohm('4.txt', npt),
    ohm('10.txt', npt),
    ohm('9.txt', npt)]

p = 2.9  # wafer resistivity in ohm cm

d = [0.35, 0.35, 0.25, 0.20, 0.18, 0.16, 0.125]  # mask diameters
from large to small (in cm) [1,6,2,3,4,10,9,8]

t = 0.020  # wafer thickness in cm

#pl.show()  # Shows Every I-V Curve (If you want to use this,
remove the # in the beginning and add # to the beginning of line
111)

###################################### Adjust The Parameters Above
##################################################


pi = ma.pi

knownr = []

for n in range(len(d)):
    knownrr = (rtfunc(rr)[n] - rsfunc(p, d, t, on)[n])
    knownr.append(knownrr)

# knownr = pc - 1/(1/4 * pi d^2) + rzero = c * pc + rzero

c = []  # c = 1/A = m in knownr = mx + R0

for n in d:
    cn = 1 / (1 / 4 * pi * n ** 2)
    c.append(cn)

lastplot(c, knownr)
```